Article

Molecular Cell

Cryo-EM of Mitotic Checkpoint Complex-Bound APC/C Reveals Reciprocal and Conformational Regulation of Ubiquitin Ligation

Graphical Abstract

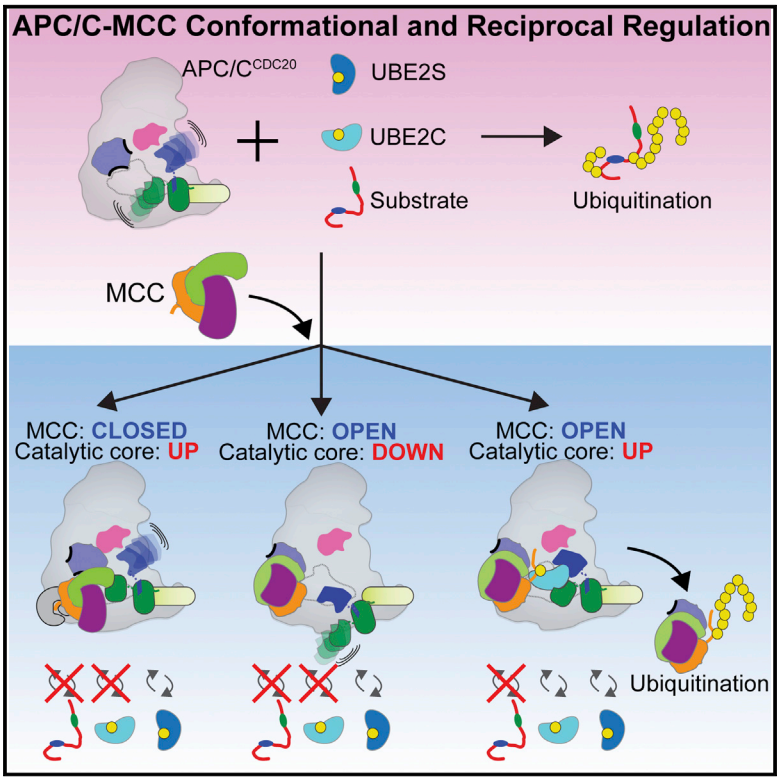

Highlights

- Cryo-EM shows reciprocal and conformational regulation of APC/C^{CDC20} and MCC
- MCC blocks APC/C^{CDC20}-binding sites for substrates such as Cyclins and Securin
- Closed APC/C^{CDC20}-MCC blocks E2 UBE2C, as during the spindle checkpoint
- Open APC/C^{CDC20}-MCC directs ubiquitination of MCC, as during checkpoint silencing

Authors

Masaya Yamaguchi,
Ryan VanderLinden,
Florian Weissmann, ...,
Jan-Michael Peters, Holger Stark,
Brenda A. Schulman

Correspondence

jan-michael.peters@imp.ac.at (J.-M.P.),
hstark1@gwdg.de (H.S.),
brenda.schulman@stjude.org (B.A.S.)

In Brief

The mitotic checkpoint complex (MCC) prevents APC/C^{CDC20}-catalyzed ubiquitination of anaphase inhibitors until all chromosomes are properly bioriented. Cryo-EM and biochemistry reveal that diverse conformations of APC/C^{CDC20}-MCC regulate E2 activation and ubiquitin targeting to ensure accurate chromosome segregation.

Accession Numbers

5KHR
5KHU

Yamaguchi et al., 2016, Molecular Cell *63*, 593–607
August 18, 2016
http://dx.doi.org/10.1016/j.molcel.2016.07.003

Molecular Cell
Article

Cryo-EM of Mitotic Checkpoint Complex-Bound APC/C Reveals Reciprocal and Conformational Regulation of Ubiquitin Ligation

Masaya Yamaguchi,[1,6] Ryan VanderLinden,[1,2,6] Florian Weissmann,[3,6] Renping Qiao,[3] Prakash Dube,[4] Nicholas G. Brown,[1] David Haselbach,[4] Wei Zhang,[5] Sachdev S. Sidhu,[5] Jan-Michael Peters,[3,*] Holger Stark,[4,*] and Brenda A. Schulman[1,2,*]
[1]Department of Structural Biology, St. Jude Children's Research Hospital, Memphis, TN 38105, USA
[2]Howard Hughes Medical Institute, St. Jude Children's Research Hospital, Memphis, TN 38105, USA
[3]Research Institute of Molecular Pathology (IMP), Vienna Biocenter (VBC), 1030 Vienna, Austria
[4]Max Planck Institute for Biophysical Chemistry, 37077 Göttingen, Germany
[5]Donnelly Centre for Cellular and Biomolecular Research and Banting and Best Department of Medical Research, University of Toronto, Toronto, ON M5S3E1, Canada
[6]Co-first author
*Correspondence: jan-michael.peters@imp.ac.at (J.-M.P.), hstark1@gwdg.de (H.S.), brenda.schulman@stjude.org (B.A.S.)
http://dx.doi.org/10.1016/j.molcel.2016.07.003

SUMMARY

The mitotic checkpoint complex (MCC) coordinates proper chromosome biorientation on the spindle with ubiquitination activities of CDC20-activated anaphase-promoting complex/cyclosome (APC/C^{CDC20}). APC/C^{CDC20} and two E2s, UBE2C and UBE2S, catalyze ubiquitination through distinct architectures for linking ubiquitin (UB) to substrates and elongating polyUB chains, respectively. MCC, which contains a second molecule of CDC20, blocks APC/C^{CDC20}-UBE2C-dependent ubiquitination of Securin and Cyclins, while differentially determining or inhibiting CDC20 ubiquitination to regulate spindle surveillance, checkpoint activation, and checkpoint termination. Here electron microscopy reveals conformational variation of APC/C^{CDC20}-MCC underlying this multifaceted regulation. MCC binds APC/C-bound CDC20 to inhibit substrate access. However, rotation about the CDC20-MCC assembly and conformational variability of APC/C modulate UBE2C-catalyzed ubiquitination of MCC's CDC20 molecule. Access of UBE2C is limiting for subsequent polyubiquitination by UBE2S. We propose that conformational dynamics of APC/C^{CDC20}-MCC modulate E2 activation and determine distinctive ubiquitination activities as part of a response mechanism ensuring accurate sister chromatid segregation.

INTRODUCTION

The massive, multisubunit E3 ligase anaphase-promoting complex/cyclosome (APC/C) initiates chromosome segregation by directing ubiquitin (UB)-mediated proteolysis of anaphase inhibitors, such as Securin, and other key mitotic regulators like Cyclins. Regulation is achieved by post-translational modifications and the coordinated action of coactivators, E2 enzymes, and inhibitors (Sivakumar and Gorbsky, 2015). APC/C is activated in prophase by phosphorylation, which allows binding to the coactivator CDC20 (Fujimitsu et al., 2016; Qiao et al., 2016; Zhang et al., 2016). CDC20 binding enables substrate binding, and it allosterically activates the catalytic core consisting of cullin (APC2) and RING (APC11) subunits (Burton et al., 2005; Chang et al., 2014; Kimata et al., 2008; Van Voorhis and Morgan, 2014; Zhang et al., 2016).

APC2 and APC11 are differentially harnessed by evolving ubiquitinated substrates and APC/C's two partner E2s, UBE2C and UBE2S, for different forms of polyubiquitination (Brown et al., 2016), with UBE2C catalyzing UB ligation directly to substrates and UBE2S extending K11-linked chains. However, accurate cell division depends on APC/C^{CDC20} waiting until all chromosomes are properly bioriented on the spindle before triggering destruction of anaphase inhibitors (Jia et al., 2013; Primorac and Musacchio, 2013). Premature chromosome segregation and aneuploidy are averted by the spindle assembly checkpoint (SAC). The SAC monitors chromosome attachment and delays anaphase by producing the mitotic checkpoint complex (MCC), which blocks APC/C^{CDC20}-dependent ubiquitination of substrates such as Securin and Cyclin B (Braunstein et al., 2007; Burton and Solomon, 2007; Fraschini et al., 2001; Hardwick et al., 2000; Herzog et al., 2009; Izawa and Pines, 2015; Kulukian et al., 2009; Sudakin et al., 2001).

Control of APC/C^{CDC20} activity in response to the status of the mitotic spindle involves tunable cycles of CDC20 synthesis and degradation, MCC assembly and disassembly, and APC/C^{CDC20}-MCC association and dissociation (Foley and Kapoor, 2013; Foster and Morgan, 2012; Jia et al., 2013; Kim and Yu, 2011; Lara-Gonzalez et al., 2012; London and Biggins, 2014; Mansfeld et al., 2011; Musacchio, 2015; Musacchio and Ciliberto, 2012; Primorac and Musacchio, 2013; Uzunova et al., 2012). During chromosome alignment, APC/C^{CDC20} remains blocked by newly produced MCC replacing that which has

dissociated. Checkpoint activation results in stabilization of MCC and APC/C^{CDC20}-MCC complexes, whereas proper chromosome biorientation leads to termination of MCC production, liberation of APC/C^{CDC20}, and dismantling of MCC.

A particularly vexing feature of checkpoint regulation is the reciprocal control of APC/C^{CDC20} and MCC (Reddy et al., 2007; Varetti et al., 2011). The evolutionarily conserved MCC core is a three-protein complex consisting of a distinct molecule of CDC20, MAD2, and BUBR1/Mad3, although MCC from some organisms, including humans, also contains BUB3 (Izawa and Pines, 2015; Jia et al., 2013; Primorac and Musacchio, 2013). On one hand, MCC acts as an inhibitor of APC/C^{CDC20} and blocks substrates. However, MCC appears to modulate activity of the priming E2, UBE2C, without impacting binding to the chain-forming E2, UBE2S (Kelly et al., 2014).

In the context of an APC/C^{CDC20}-MCC complex, CDC20 can be ubiquitinated depending on the status of the checkpoint (Eytan et al., 2013; Ge et al., 2009; Jia et al., 2011, 2013; Mansfeld et al., 2011; Miniowitz-Shemtov et al., 2010; Musacchio, 2015; Musacchio and Ciliberto, 2012; Nilsson et al., 2008; Pan and Chen, 2004; Reddy et al., 2007; Uzunova et al., 2012; Varetti et al., 2011). Although CDC20 is a very short-lived protein, mechanisms and consequences of CDC20 ubiquitination remain under investigation. Ubiquitination may prevent accumulation of excess CDC20, potentially to avert mitotic slippage (Mansfeld et al., 2011; Nilsson et al., 2008). However, high UBE2C activity correlates with CDC20 ubiquitination and MCC dissociation from APC/C, suggesting that UBE2C-mediated CDC20 ubiquitination contributes to checkpoint termination (Foster and Morgan, 2012; Reddy et al., 2007; Uzunova et al., 2012; Varetti et al., 2011). Accordingly, knocking down UBE2C and UBE2S decreased the efficiency of release from the SAC and delayed progress from nuclear envelope breakdown to anaphase (Garnett et al., 2009; Jia et al., 2011; Kelly et al., 2014; Varetti et al., 2011; Wild et al., 2016; Williamson et al., 2009). Furthermore, CDC20 was stabilized and MCC accumulated on APC/C in checkpoint-arrested cells depleted for the APC15 subunit, or the corresponding Mnd2 in yeast (Foster and Morgan, 2012; Mansfeld et al., 2011; Uzunova et al., 2012). Notably, the only obvious catalytic defect of APC/C lacking APC15 (APC/CΔ15) was strikingly impaired CDC20 ubiquitination in the presence of MCC (Foster and Morgan, 2012; Uzunova et al., 2012).

Here we use electron microscopy (EM) and biochemistry to dissect regulation of APC/C^{CDC20} and MCC via ubiquitination by UBE2C and UBE2S. For clarity, we refer to the APC/C-bound activator CDC20 as CDC20$_A$ (i.e., in APC/C^{CDC20}) and that in MCC as CDC20$_M$. While MCC uniformly blocks substrate binding to APC/C^{CDC20}, multiple conformations of APC/C^{CDC20}-MCC, with rotation of the CDC20$_A$-MCC assembly relative to APC/C and different positions for the APC2-APC11 catalytic core, determine if CDC20$_M$ is a substrate of UBE2C. Notably, the distribution of MCC complexes with APC/C^{CDC20} lacking APC15 (APC/C^{CDC20}Δ15) is shifted toward configurations that block UBE2C activation, while UBE2S binding and di-UB synthesis capabilities remain intact to presumably mediate rapid polyubiquitination after CDC20 is modified by UBE2C. We propose that biasing APC/C^{CDC20}-MCC conformation toggles ubiquitination of CDC20 as part of a dynamic response mechanism that can either sustain the SAC or trigger rapid onset of anaphase.

RESULTS

EM Reconstructions Reveal Conformational Variability of APC/C^{CDC20}-MCC

We established recombinant systems for APC/C^{CDC20} (with glutamate replacements for 100 Ser/Thr sites of mitotic phosphorylation) that mimics the endogenous complex (Qiao et al., 2016; Weissmann et al., 2016), and for MCC by coexpressing its subunits in insect cells (Figures S1A–S1C). This allowed reconstituting MCC inhibition of UB ligation to fluorescent versions of Cyclin B's N-terminal domain (CycB^{N*}), Securin*, and Cyclin A* by APC/C^{CDC20}, UBE2C, and UBE2S (Figure 1A).

To gain structural insights into regulation, we analyzed APC/C^{CDC20}-MCC by cryo-EM. Three-dimensional (3D) classification revealed several sub-populations with two globally distinctive configurations we termed "closed" and "open", which themselves are defined by multiple classes presumably reflecting their conformational dynamics. Cryo-EM reconstructions for APC/C^{CDC20}-MCC in the closed and open configurations were refined at resolutions of 9 and 10 Å, respectively (Table S1). Docking prior structures of human APC/C^{CDC20} and *S. pombe* MCC core (44% identical to human CDC20-BUBR1-MAD2) into the maps showed the arrangements of the two molecules of CDC20, with A bound to APC/C via activator-binding sites and the other (M) in MCC (Chao et al., 2012; Izawa and Pines, 2015; Primorac and Musacchio, 2013; Zhang et al., 2016).

The distinct conformations display substantially different orientations of CDC20$_A$-MCC with respect to APC/C (Figures 1B and 1C; Movies S1 and S2). In the closed conformation, MCC fills the central cavity by engaging APC/C^{CDC20} on three sides. A continuous surface from CDC20$_M$ and BUBR1 engages CDC20A. CDC20$_M$ contacts the available protomer (A) of the APC8 homodimer. BUBR1 interacts with the APC2-APC11 cullin-RING catalytic core. When open, the CDC20$_A$-MCC assembly is preserved but is localized away from the catalytic core.

Only the MCC core corresponding to CDC20-BUBR1-MAD2 was readily visible in the maps, despite the presence of BUB3 in the complex (Figure S1A). To validate this, we purified an MCC core complex that inhibited substrate ubiquitination as described (Izawa and Pines, 2015), with only slightly lower efficiency than full MCC in our assays (Figure 1A). Upon performing side-by-side negative-stain EM analyses on APC/C^{CDC20} bound to full or core MCC, the resultant maps were superimposable, and there were not obvious major differences in the ratios of closed and open configurations among matched preps with or without BUB3 (Figures 1D–1G and S1B–S1D). For comparison, retrospective inspection of the EM map from endogenous APC/C^{CDC20}-MCC further validated that only the MCC core is apparent, even in the presence of BUB3 (Figure 1H) (Herzog et al., 2009). This is consistent with conservation of key APC/C^{CDC20}-MCC features across eukaryotes, as MCC lacks BUB3 in some organisms (Vanoosthuyse et al., 2009; Windecker et al., 2009). We speculate that BUB3 may be relatively flexibly tethered to APC/C^{CDC20}-MCC, and, thus, all subsequent EM studies were performed with the MCC core complex unless otherwise stated (Table S1).

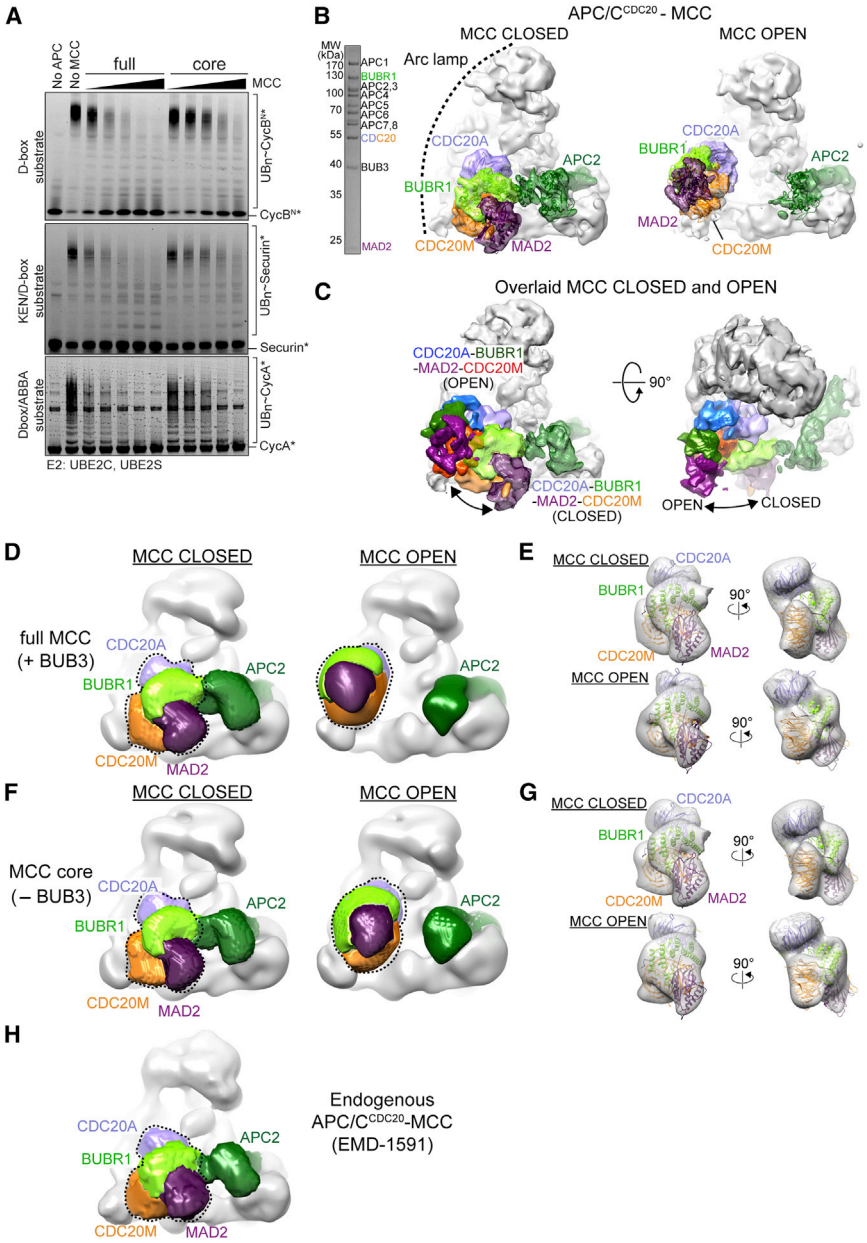

Figure 1. Multiple APC/C^{CDC20}-MCC Conformations Revealed by EM

(A) Ubiquitination of fluorescent CycB^{N*}, Securin*, and CycA* by APC/C^{CDC20}, titrating increasing concentrations of either full or core (CDC20$_M$-BUBR1-MAD2) MCC, is shown.

(B) Cryo-EM reconstructions show representative APC/C^{CDC20}-MCC closed (left) and open (right) conformations refined at 9- and 10-Å resolution, respectively (SDS-PAGE gel of APC/C^{CDC20}-MCC, left).

(C) Superimposition of cryo-EM maps for closed and open conformations of APC/C^{CDC20}-MCC is shown.

(D) Negative-stain EM reconstructions show APC/C^{CDC20} in complex with full MCC, which contains BUB3.

(E) The overall CDC20$_A$-MCC core assembly from docked crystal structures (Chao et al., 2012; Tian et al., 2012) is observed in both the closed and open configurations of APC/C^{CDC20}-MCC.

(F) Shown as in (D), except with core MCC (CDC20$_M$-BUBR1-MAD2) lacking BUB3.

(G) Shown as in (E), except with CDC20$_A$-MCC core assembly-docked negative-stain EM maps from (F).

(H) Negative-stain EM reconstruction of endogenous MCC-bound APC/C (Electron Microscopy Data Bank: EMD-1591) (Herzog et al., 2009) is shown.

See also Figure S1, Tables S1 and S2, and Movies S1, S2, and S3.

Reexamination of the published negative-stain EM map of APC/C-MCC purified from checkpoint-arrested HeLa cells revealed that the dominant population (56%) corresponds to the closed configuration, which may reflect higher propensity for purification due to additional contacts, increased homogeneity of the closed configuration, or relative stabilization of the closed configuration during the checkpoint (Figure 1H) (Herzog et al., 2009). Blurring of the MCC moiety in the published map generated from unstained cryo-EM data on endogenous APC/C^{CDC20}-MCC may reflect conformational heterogeneity arising from the dynamic configurations (Herzog et al., 2009). Superimposing the EM maps corresponding to different 3D classes suggested a continuum of conformations where the CDC20$_A$-MCC assembly rotates to APC/C. Notably, the APC2-APC11 catalytic core also exhibited conformational heterogeneity between the closed and open configurations and among open 3D classes even from a single sample (Movie S3).

MCC Inhibition of Substrate Ubiquitination Revealed by Side-by-Side Comparison of APC/C and APC/C^{CDC20} Complexes with Substrate or MCC

Cryo-EM reconstructions were aligned for phosphorylated apo APC/C (Figure 2A) (Zhang et al., 2016), substrate-bound APC/C^{CDC20} (Figure 2B) (Zhang et al., 2016), and closed and open conformations of APC/C^{CDC20}-MCC (Figures 2C and 2D). Side-by-side comparison showed common mechanisms by which the closed and open configurations hijack substrate-binding sites on APC/C^{CDC20}, while differing in their interactions with the catalytic core.

Prior structural data showed how CDC20 can allosterically activate E3 ligase activity. In the absence of CDC20, the canonical E2-binding site on APC11's RING domain is masked, because the APC2-APC11 cullin-RING catalytic core occupies a down position (Figure 2A) (Chang et al., 2014). However, in the cryo-EM maps for an APC/C^{CDC20}-substrate complex, the APC2-APC11 catalytic core is relatively up and freed from autoinhibition, and it is visible only at lower contour and

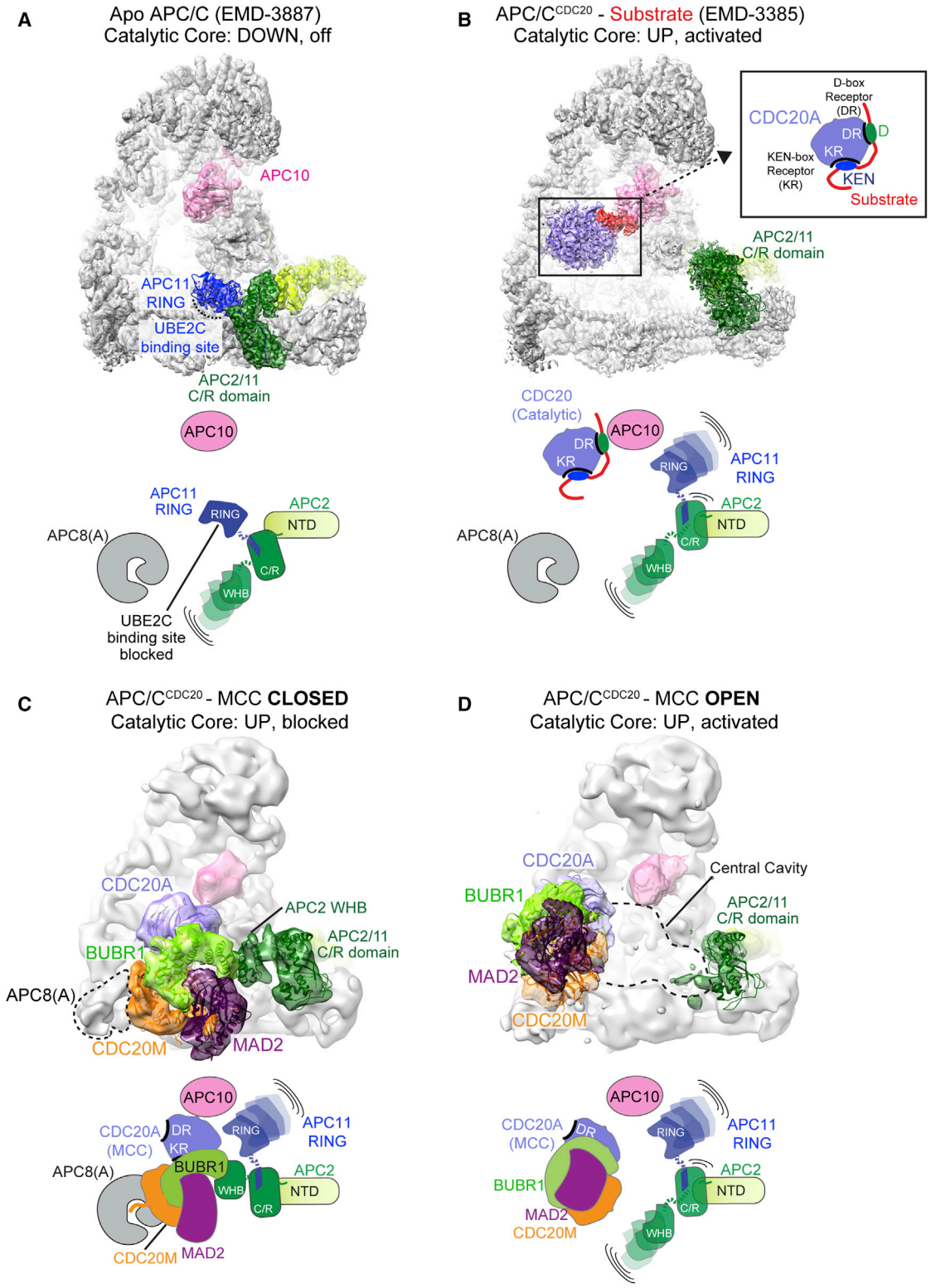

Figure 2. Snapshots of Distinct APC/C Conformations Associated with Activation by CDC20 and Modulation by MCC

(A) Prior cryo-EM map of apo-phosphorylated APC/C (Zhang et al., 2016) showed the APC2 (green)-APC11 (blue) catalytic core as down, blocking the canonical E2-binding site on APC11's RING used by UBE2C. Cartoon depicts key elements related to MCC functions.

(legend continued on next page)

resolution presumably due to mobility (Figure 2B) (Zhang et al., 2016). This increases catalytic competence, because three domains of the catalytic core (the intermolecular cullin/RING C/R domain, the APC2 C-terminal WHB domain, and the APC11 C-terminal RING domain) are harnessed into different catalytic architectures for substrate ubiquitination by UBE2C and UB chain elongation by UBE2S (Brown et al., 2015, 2016; Chang et al., 2015).

In the closed configuration, MCC captures the WHB domain from APC2, which is enabled by upward positioning of the C/R domain (Figure 2C). When APC/C^{CDC20}-MCC is open, the catalytic core is fully available, localized upward, and less visible, consistent with competence for binding to UBE2C (Figure 2D) (Brown et al., 2015, 2016; Chang et al., 2015).

In both configurations, MCC masks substrate-binding sites by CDC20$_M$ and BUBR1 encasing the top side of CDC20$_A$'s β-propeller (Figures 1 and 2). Also, relative rotation of CDC20$_A$'s β-propeller dismantles the D-box-binding site between CDC20$_A$ and APC10 (Figures 2B–2D) (Herzog et al., 2009).

In separate sections below, we describe EM data (Table S1) and biochemistry defining elements mediating MCC inhibition of APC/C^{CDC20}, mechanisms of CDC20 ubiquitination in the context of APC/C^{CDC20}-MCC, and how APC/C^{CDC20}-MCC structure and activity are modulated in the absence of APC15.

APC/C^{CDC20}-MCC Elements Inhibiting Substrate Ubiquitination

The highest resolution cryo-EM map obtained during the course of these studies was for the closed configuration with an APC/C^{CDC20} mutant lacking APC15 (Figure S2A; Table S1; 4.8-Å resolution by gold-standard Fourier shell correlation). Here we depict the CDC20$_A$-MCC interface from this map, while effects of deleting APC15 are described in separate sections. Lower resolution for the CDC20$_A$-MCC assembly of ≈6.5 Å presumably reflects relative mobility, but it was sufficient to dock prior high-resolution structures of MCC subunits for visualizing elements mimicking substrate D-, KEN-, and ABBA/Phe-box motifs (Figures 3, S2, and S3).

On one edge of CDC20$_A$, there is potentially weak density in the D-box-binding site, and strong density for a Cys-Arg-Tyr (CRY) box immediately preceding CDC20$_M$'s propeller domain (Figures 3A and 3B). The other edge of CDC20$_A$ apparently binds an ABBA/Phe-box-like motif (Di Fiore et al., 2015; Diaz-Martinez et al., 2015), which continues into a pre-KEN sequence and ultimately a KEN-box that are sandwiched between the CDC20$_A$ propeller and the CDC20$_M$/BUBR1 surface from MCC (Figures 3A, 3C, and S3A). Indeed, prior studies had identified D1 and KEN2 motifs in BUBR1 and the corresponding D- and KEN-box receptor sites on CDC20$_A$ as important for MCC binding to APC/C (Izawa and Pines, 2015). We further validated the cryo-EM data by testing effects of mutating BUBR1's D1, ABBA-like, pre-KEN, and KEN2 motifs and CDC20$_M$'s CRY box in MCC, as well as the KEN receptor in CDC20$_A$. All these structure-based mutations thwarted MCC inhibition of substrate ubiquitination (Figures 3D, 3E, and S3B).

APC/C^{CDC20}-MCC in the Open Configuration Is Structurally Poised for UBE2C-Dependent Ubiquitination of CDC20$_M$

The two APC/C^{CDC20}-MCC conformations present an intriguing dichotomy for the catalytic core. In particular, with the CDC20$_A$-MCC assembly swung open, APC/C's central cavity is vacant and, in principle, could accommodate UBE2C (Figure 2D) (Brown et al., 2015; Chang et al., 2015). Although previous studies monitoring cellular CDC20 ubiquitination during the spindle assembly checkpoint could not distinguish between CDC20$_A$ and CDC20$_M$ (Foster and Morgan, 2012; Mansfeld et al., 2011; Uzunova et al., 2012), we used methylated UB that cannot form chains to directly probe targeting. CDC20$_A$ was distinguished by an N-terminal Myc tag and CDC20$_M$ by a FLAG tag (Figure 4A). Adding MCC to APC/C^{CDC20} and the E2 UBE2C resulted in CDC20$_M$ ubiquitination and decreased modification of CDC20$_A$ (Figure 4B). CDC20$_M$ ubiquitination was decreased by mutating a pair of known CDC20 ubiquitination sites (Lys485 and 490) within MCC (Figure 4C) (Mansfeld et al., 2011; www.phosphosite.org).

To visualize the APC/C^{CDC20}-MCC-UBE2C architecture poised for CDC20$_M$ ubiquitination, we modified our published approach to capture targeting by UBE2C (Brown et al., 2015, 2016). Briefly, the homobifunctional crosslinker BMOE joined UBE2C's active site Cys with a Cys corresponding to Lys490 in a modified CDC20$_M$ (Figure 4D). A purified BMOE-linked MCC-UBE2C complex was assembled with APC/C^{CDC20} for structural analysis by negative-stain EM (Figures 4D and 4E). The EM reconstruction shows the open configuration. Docking prior crystal structures shows how APC2's WHB and APC11's RING domains co-engage UBE2C (Brown et al., 2014, 2015). This places UBE2C in a parallel location as poised for substrate ubiquitination, except UBE2C's active site is juxtaposed with CDC20$_M$ (Figures 4E and S4) (Brown et al., 2015; Chang et al., 2015). We mutationally tested the mechanism, removing APC2's UBE2C-binding WHB domain or APC11's UBE2C-activating RING domain from APC/C^{CDC20}, or with UBE2C F53D and Y91D point mutations in the APC2- and APC11-binding sites, respectively (Brown et al., 2014, 2015). The mutants eliminated CDC20$_M$ ubiquitination, suggesting a crucial role for the APC2-APC11 cullin-RING mechanism activating UBE2C∼UB (Figures 4F and S4) (Brown et al., 2015).

(B) Prior cryo-EM map for APC/C^{CDC20}-substrate complex (Zhang et al., 2016), showing substrate D-box (red) co-recruited to CDC20's propeller (violet) and APC10 (pink). The catalytic core is activated by increased conformational mobility. D-box receptor (DR) and KEN-box receptor (KR) sites are indicated.

(C) Cryo-EM map showing closed configuration of APC/C^{CDC20}-MCC. MCC blocks substrate-binding sites and contacts APC2's UBE2C-binding WHB domain and APC8 (protomer A).

(D) Cryo-EM map showing open configuration of APC/C^{CDC20}-MCC. MCC blocks substrate-binding sites. APC/C's central cavity is vacant and APC2-APC11 catalytic core is activated and less resolved, suggestive of mobiltity.

See also Figure S2.

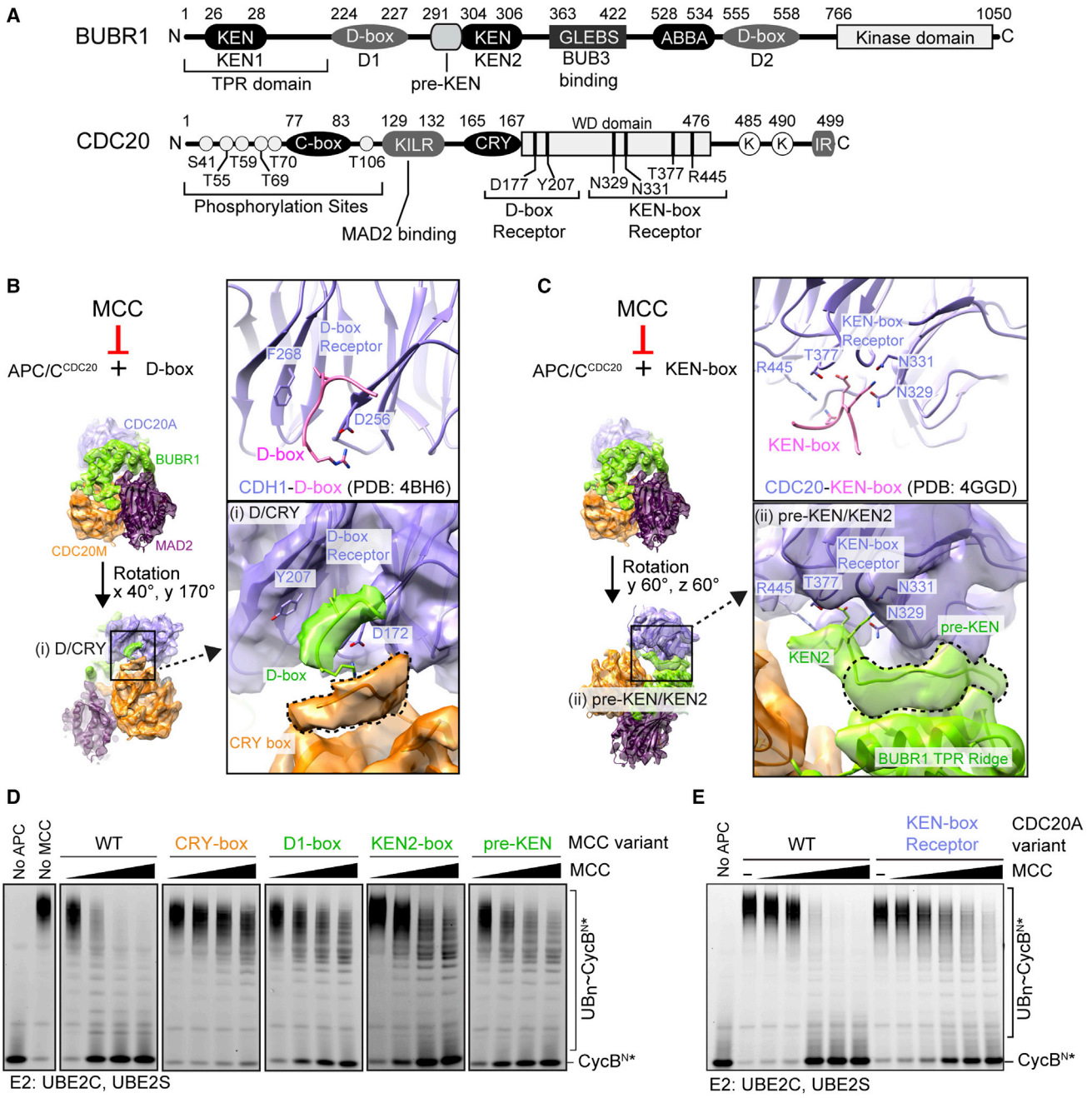

Figure 3. Multiple Related Elements Mediate Substrate and MCC Association with $CDC20_A$

(A) Schemes of BUBR1 and CDC20 motifs are shown.

(B) Close-up views of coactivator-D/CRY-box interactions are aligned for crystal structure of CDH1-D-box (He et al., 2013) and cryo-EM map of APC/C^{CDC20}Δ15-MCC (closed, 4.8-Å resolution) to show density for $CDC20_M$ CRY-box and D-box receptor region of $CDC20_A$.

(C) Close-up views show CDC20-KEN-box interactions aligned from crystal structure (Tian et al., 2012) and cryo-EM map of APC/C^{CDC20}Δ15-MCC (closed configuration, 4.8-Å resolution).

(D) Mutations in key MCC elements impair inhibition, detected by titrating increasing concentrations of MCC into reactions monitoring APC/C^{CDC20}-mediated ubiquitination of the fluorescent substrate $CycB^{N*}$.

(E) Mutations in $CDC20_A$ KEN-box-binding site impair MCC-mediated inhibition, detected by reactions as in (D). Note that $CycB^{N*}$ has a D-box, but not a KEN-box, so its ubiquitination in the absence of MCC is not substantially impaired by $CDC20_A$ KEN-box receptor mutant.

See also Figure S3.

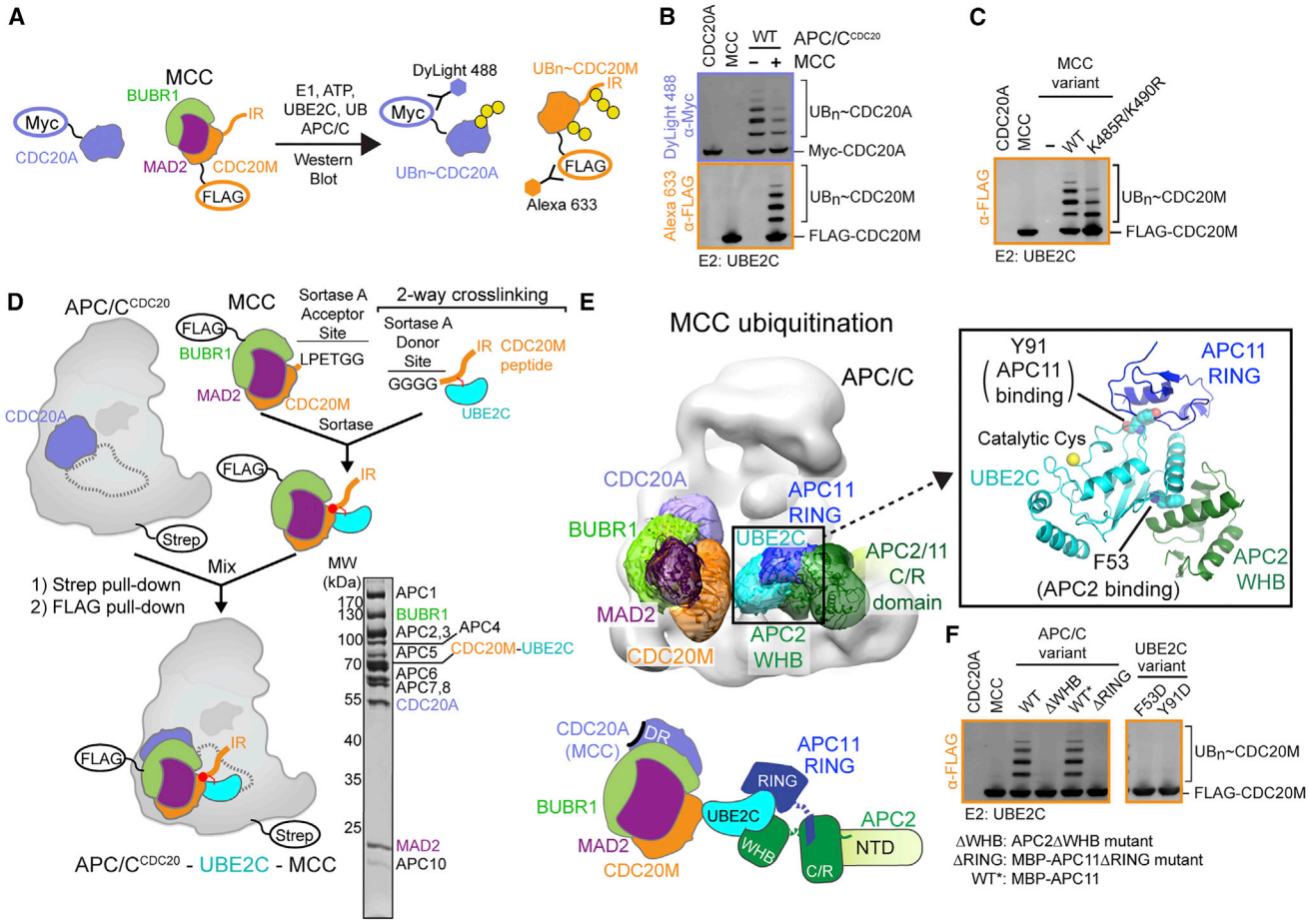

Figure 4. APC/C^{CDC20}-MCC Open Configuration Directs UBE2C-Catalyzed Ubiquitination of CDC20$_M$

(A) Scheme shows two-color western blot distinguishing CDC20$_A$ and CDC20$_M$ in ubiquitination assays.

(B) APC/C^{CDC20} and UBE2C-dependent modification of CDC20 was monitored in reactions with methyl-UB that can be linked to substrate, but cannot form chains.

(C) Reactions as in (B) show roles of known CDC20 ubiquitination sites by comparing APC/C^{CDC20} and UBE2C-dependent ubiquitination for WT and K485R/K490R CDC20$_M$.

(D) Scheme for purifying APC/C^{CDC20}-UBE2C-MCC core, with CDC20$_M$ residue 490 (corresponding to ubiquitination site) crosslinked to active site of UBE2C, is shown.

(E) Negative-stain EM reconstruction of APC/C^{CDC20}-UBE2C-MCC core representing CDC20$_M$ ubiquitination, with CDC20$_A$-MCC rotated in the open configuration. Inset: close-up of model shows key elements to recruit/activate/position UBE2C from prior crystal structures that are docked in EM map (Brown et al., 2014, 2015).

(F) Assay as in (B) tested cullin (APC2) and RING (APC11) architecture in recruiting/positioning/activating UBE2C for UB ligation to CDC20$_M$, through deleting UBE2C-binding (APC2 WHB) and -activating (APC11 RING) domains from APC/C, or mutating corresponding contact residues from UBE2C (F53 and Y91, respectively) (Brown et al., 2014).

See also Figure S4.

Cryo-EM Maps of APC/C^{CDC20}-MCC without the APC15 Subunit Show a Shift toward Conformations Inhibiting the Activation of UBE2C

To understand how APC/C^{CDC20}-MCC can be regulated, we considered that depleting the APC/C subunit APC15 selectively impairs CDC20 ubiquitination during checkpoint regulation (Foster and Morgan, 2012; Mansfeld et al., 2011; Uzunova et al., 2012). We discovered this is an intrinsic property of APC/C, because, in comparison to the wild-type (WT) complex, recombinant APC/C^{CDC20} prepared without APC15 (APC/C^{CDC20}Δ15) retained substrate ubiquitination activity that was inhibited by MCC, but MCC ubiquitination was selectively impaired (Figures 5A, 5B, and S5A).

To compare structural effects of deleting APC15 on substrate ubiquitination versus on interactions with MCC, we first adapted our method for visualizing an assembly mimicking an APC/C^{CDH1}-UBE2C∼UB-substrate intermediate (Brown et al., 2015). We determined a cryo-EM reconstruction of APC/C^{CDC20}Δ15 bound to a three-way crosslinked complex linking the preferred ubiquitination site in a substrate, UBE2C, and a donor UB (6.1-Å resolution, gold-standard Fourier shell correlation; Figures 5C and S5B). In the maps, the most static regions extend to ≈4 Å

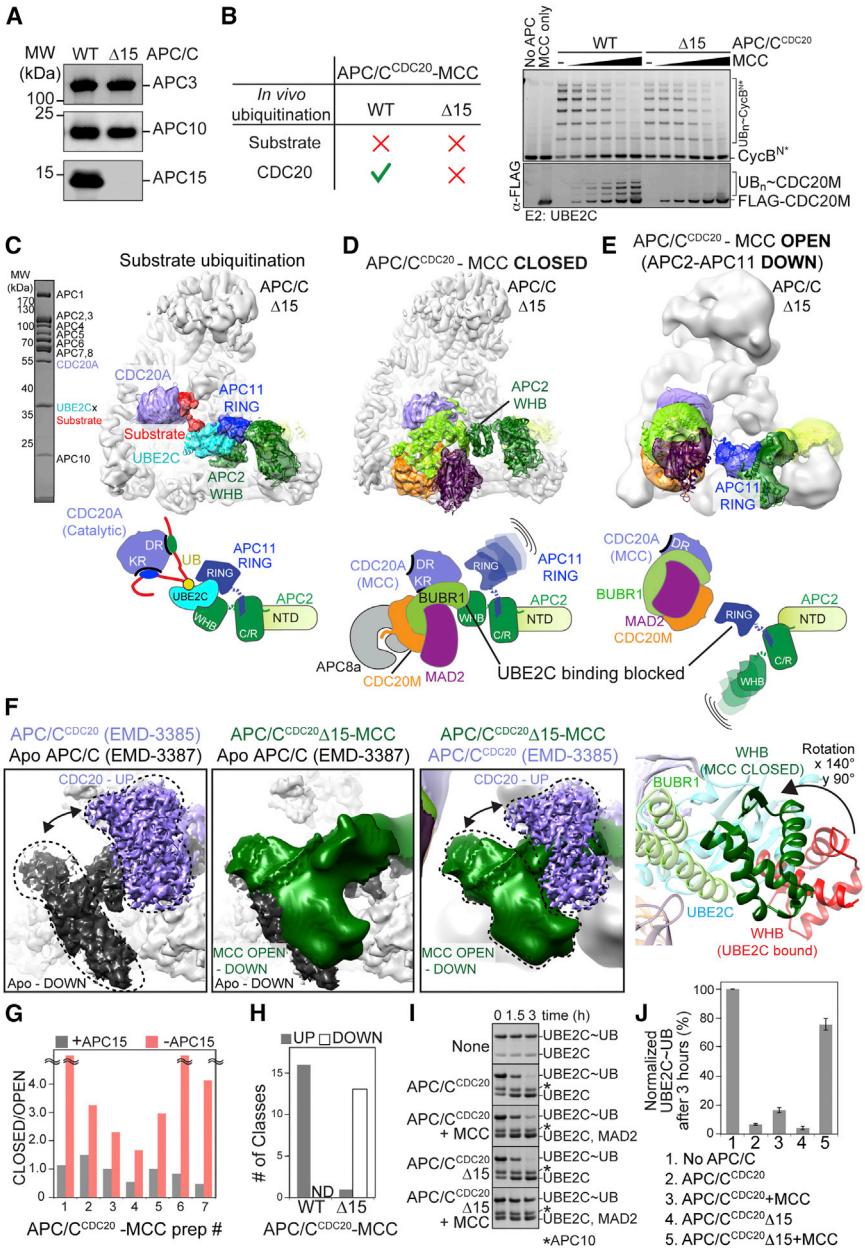

Figure 5. Deletion of APC15 Influences APC/C^{CDC20}-MCC Conformational Regulation and Activity with the E2 UBE2C

(A) Western blots (anti-APC3, -APC10, and -APC15) confirm lack of APC15 in recombinant APC/C^{CDC20}Δ15 compared to WT control.

(B) Recombinant APC/C^{CDC20}Δ15 recapitulates key endogenous properties. Left: summary from Foster and Morgan (2012), Mansfeld et al. (2011), and Uzunova et al. (2012) is shown. Right: deleting APC15 from recombinant APC/C^{CDC20} has no obvious impact on UBE2C-dependent substrate ubiquitination in the absence of MCC but impairs ubiquitination of CDC20$_M$ from MCC, tested by simultaneous detection of fluorescent CycB^{N*} substrate and FLAG-CDC20$_M$ in reaction.

(C) Cryo-EM map of APC/C^{CDC20}Δ15 complex representing substrate ubiquitination with UBE2C (UBE2C active site crosslinked to substrate, 6.1-Å resolution, SDS-PAGE gel, left). Cartoon of catalytic architecture for substrate ubiquitination is shown below.

(D) Cryo-EM map shows APC/C^{CDC20}Δ15-MCC in closed configuration (4.8-Å resolution), resolving elements blocking substrate binding and inhibiting APC/C catalytic core in the up (activated) position.

(E) Cryo-EM map showing APC/C^{CDC20}Δ15-MCC in distinctive open configuration (9-Å resolution) with catalytic core in inactive down position. The UBE2C-binding site on APC11 RING domain is blocked with APC2-APC11 in down position previously described for apo-APC/C (Chang et al., 2014; Zhang et al., 2016).

(F) The left three panels show side-by-side pairwise comparison of density corresponding to APC2-APC11 catalytic core after superimposing cryo-EM maps for apo APC/C and APC/C^{CDC20} (Zhang et al., 2016) and APC/C^{CDC20}Δ15-MCC in the atypical inactive open configuration shown in (E). CDC20$_A$ binding to apo APC/C typically induces repositioning of the APC2-APC11 catalytic core from a down position to an up orientation, which enables UBE2C to bind APC2's WHB and APC11's RING domains (Brown et al., 2015; Chang et al., 2015; Zhang et al., 2016). The minor population of APC/C^{CDC20}Δ15-MCC in the open configuration is inactive due to the catalytic core occupying the down orientation. Right: APC2 WHB domain rotation between engaging MCC in closed conformation (green) or UBE2C for UB ligation (red).

(G) The ratio of CDC20$_A$-MCC populations in closed versus open configurations observed in negative-stain EM reconstructions of seven matched purifications of MCC bound to WT or Δ15 APC/C^{CDC20} (Table S2). Samples with no open classes are denoted (≈).

(H) Among the classes in open configurations analyzed in (G), the poplulations with the APC2-APC11 catalytic core in activated up versus inactive down positions were compared for WT or Δ15 APC/C^{CDC20} (Table S3).

(I) Comparing effects of MCC on WT or APC/C^{CDC20}Δ15-stimulated activation of UBE2C∼UB, as monitored by hydrolysis of oxyester-linked UBE2C(catalytic Cys-to-Ser)∼UB into free UBE2C and UB, is shown.

(J) Comparing MCC inhibition of WT or APC/C^{CDC20}Δ15-stimulated activation of UBE2C∼UB, by quantification of UBE2C∼UB remaining after 3 hr from experiments as in (I), is shown. Error, SEM; n = 3.

See also Figure S5 and Tables S2 and S3.

in resolution, with a lower resolution for catalytic core presumably arising from dynamic properties required for ubiquitination, The map resembled that representing an APC/C^{CDH1}-UBE2C∼UB-substrate intermediate, with UBE2C bound to APC2-APC11 adjacent to substrate and with the donor UB not visible presumably due to conformational flexibility (Figures S5C and S5D) (Brown et al., 2014, 2015; Zhang et al., 2016). The most obvious effects of deleting APC15 were the lack of

APC15 and disappearance of density for and rearrangement of APC15-binding helices from APC5 (Figure S5E).

We analyzed conformations of APC/C^{CDC20}Δ15-MCC by cryo-EM to understand how ubiquitination is impaired. Maps corresponding to closed and open configurations were refined at overall resolutions of 4.8 and 9 Å, respectively (Figures 5D, 5E, and S2A). In comparison to the WT complex, the complex lacking APC15 showed an obvious increase in the population of the CDC20$_M$-MCC assembly in the closed configuration, accompanied by relative rotation in APC4/APC5 regions (Figure S5E). This would block binding to UBE2C due to BUBR1 hijacking the WHB domain from APC2 (Figures 5D and 5F). UBE2C activation also was blocked in the less populated class with MCC in the open orientation, because APC2-APC11 was in the down position typically observed in apo-APC/C, which occludes UBE2C binding to the RING (Figures 2A, 5E, and 5F).

We tested if deleting APC15 indeed would hinder APC/C^{CDC20}-MCC-dependent activation of UBE2C. First, we obtained structural data by collecting negative-stain EM datasets, calculating maps, and quantifying populations in different conformations for 14 samples from seven matched preps with or without APC15. In the preps lacking APC15, the proportion forming the closed configuration was relatively increased, while those classes with the open CDC20$_A$-MCC configuration predominantly displayed the catalytic core in the down orientation blocked for UBE2C binding (Figures 5G and 5H; Tables S2 and S3). Second, we directly tested effects of deleting APC15 and/or adding MCC on the activation of UBE2C∼UB, by monitoring hydrolysis of an oxyester-bonded UBE2C∼UB conjugate with UB linked to Ser replacing UBE2C's catalytic Cys. In agreement with the structural data, adding APC/C^{CDC20} stimulated hydrolysis of the oxyester-bonded UBE2C∼UB conjugate irrespective of the presence or absence of APC15, while deleting APC15 enhanced inhibition by MCC (Figures 5I and 5J).

Although activity was greatly reduced, low-level hydrolysis of UBE2C∼UB (Figures 5I and 5J) raised the possibility that APC15 is not absolutely required for APC/C^{CDC20}-MCC to adopt a conformation that activates UBE2C∼UB. This may be enhanced or more detectable at high protein concentrations, such as those used in the hydrolysis assay. To test if APC/C^{CDC20}Δ15-MCC can indeed attain an active conformation with UBE2C, we assembled the crosslinked MCC-UBE2C complex with APC/C^{CDC20}Δ15 for structural analysis by negative-stain EM (Figure 6A). The map was strikingly similar to that from the corresponding complex with WT APC/C^{CDC20} (Figure 4E). Overall, the data suggest that APC/C^{CDC20}Δ15-MCC can, in principle, activate UBE2C∼UB but that the active conformation is not preferred.

Since the EM maps of APC/C^{CDC20}Δ15-MCC in the closed configuration uniformly showed APC2-APC11 in the activated up location but with UBE2C access blocked by MCC, we hypothesized that mutations disrupting key interactions unique to the closed configuration should enable activation of UBE2C∼UB and ubiquitination of CDC20$_M$, even by APC/C^{CDC20}Δ15. One interaction unique to the closed configuration involved MCC hijacking the UBE2C-binding surface of APC2's WHB domain (Figures 6A–6C). Another involved peptide-like density terminating in the available tetratricopeptide repeat (TPR) groove from APC8 (protomer A of the APC8 homodimer) (Figure 6D). We attributed this density to CDC20$_M$'s Ile-Arg (IR) tail, due to striking similarity to IR tails from APC10, CDH1, and CDC20$_A$ bound to TPR grooves from the two APC3 protomers (Figure S5F) (Chang et al., 2015; Zhang et al., 2016). Also, APC8$_A$ is, in principle, competent to bind an Ile and Arg, as protomer B contacts such residues within a coactivator's C-box motif (Chang et al., 2015; Zhang et al., 2016) (Figure S5F), while APC8$_A$ is poised to bind CDC20$_M$'s IR tail with MCC positioned in the closed configuration. Indeed, structure-based mutations in the BUBR1 surface that binds the APC2 WHB domain, or in CDC20$_M$'s IR tail, substantially restored the ability of APC/C^{CDC20}Δ15 to hydrolyze UBE2C∼UB in the presence of MCC (Figures 6E–6H) and to catalyze CDC20$_M$ ubiquitination (Figures 6I and 6J).

UBE2S-Dependent UB-Chain Synthesis in the Presence of MCC

To understand how MCC binding would affect UB chain formation, we inspected the cryo-EM maps for potential to form the specialized APC/C architecture juxtaposing UBE2S's active site with an acceptor UB. A prior cryo-EM reconstruction, obtained by crosslinking UBE2S's catalytic Cys to a substrate-fused UB variant (UBv) with enhanced affinity for the acceptor UB-binding site, indicated that UB chain elongation by UBE2S involves a completely different catalytic architecture from that activating UBE2C (Brown et al., 2016). Instead, UBE2S's C-terminal peptide (CTP) binds an APC2/APC4 groove, while UBE2S's catalytic domain contacts a pair of APC2 C/R domain helices. The unique interactions direct UBE2S's active site toward an acceptor UB recruited to a distinct APC11 RING surface (Brown et al., 2014, 2016; Kelly et al., 2014). Notably, prior data showed that MCC did not inhibit UBE2S-dependent synthesis of unanchored diUB chains with endogenous APC/C^{CDC20} (Kelly et al., 2014).

Even in the closed configuration of APC/C^{CDC20}-MCC, the UBE2S and acceptor UB-binding sites appeared available (Figures 7A and S6A) (Kelly et al., 2014). To test if UBE2S activity is spared with MCC predominantly bound in the closed configuration, we examined UBE2S-dependent UB transfer to a fluorescein-labeled acceptor UB*, and we saw no defect from deleting APC15 (Figure 7B). To visualize this, we adapted our published approach and performed cryo-EM on APC/C^{CDC20}Δ15-MCC bound to a complex with UBE2S's catalytic Cys crosslinked to the UBv as a proxy for an acceptor UB (Brown et al., 2016) (Figure 7C). A map for the closed configuration was refined at 5.7-Å resolution, which allowed placement of APC/C^{CDC20}Δ15-MCC, while the local resolution for the catalytic core was ≈10 Å (Figures 7D, S6A, and S6B; Table S1). The position of UBE2S-UBv was approximated based on prior cryo-EM data where UBE2S was more avidly anchored with the Ubv fused to a substrate (Figures 7D and S6A) (Brown et al., 2016).

The structural data confirmed that MCC blocks substrate-binding sites on CDC20$_A$ while allowing UBE2S placement adjacent to the UB-binding site on APC11's RING domain (Figure 7D). This led to several predictions. First, UBE2S should extend polyUB chains initiated by UBE2C and APC/C^{CDC20}-MCC. We confirmed this for CDC20$_M$, as higher molecular weight conjugates were observed upon adding UBE2S, but there was no

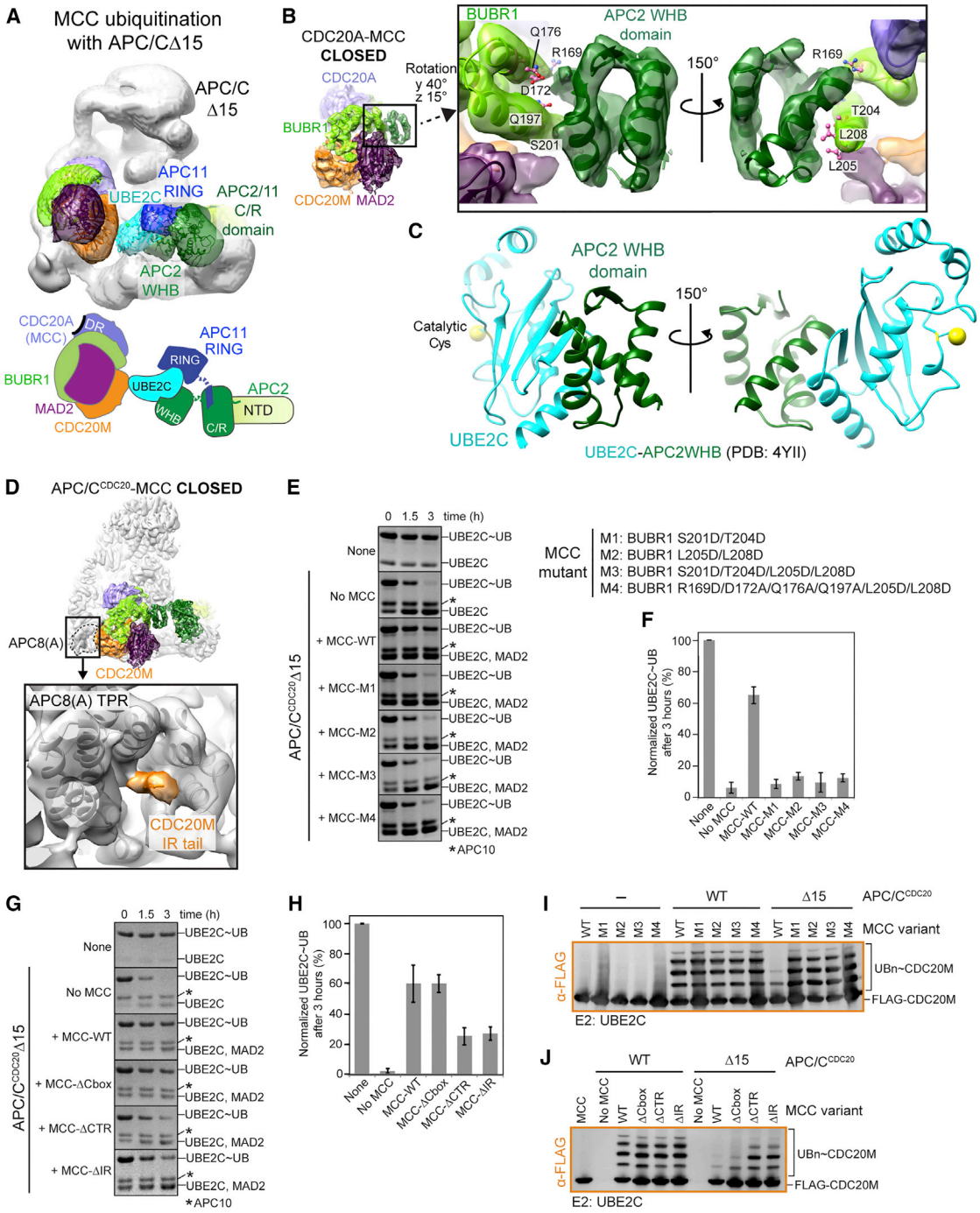

Figure 6. Elements Distinctly Mediating MCC Interactions with APC/C Subunits in Closed Configuration Determine Inhibition of $CDC20_M$ Ubiquitination

(A) APC15 is not absolutely required for APC/C^{CDC20}-UBE2C to adopt catalytic architecture for $CDC20_M$ ubiquitination. Negative-stain EM reconstruction of APC/C^{CDC20}Δ15-UBE2C-MCC core shows that forcing juxtaposition of UBE2C and $CDC20_M$ by crosslinking enables visualizing catalytic assembly as in Figure 4E.

(B) Close-up view shows BUBR1-APC2 WHB domain interactions distinctive for the closed configuration of APC/C^{CDC20}-MCC, with crystal structures (Bolanos-Garcia et al., 2011; Brown et al., 2015) docked in cryo-EM map from APC/C^{CDC20}Δ15-MCC and showing BUBR1 residues mutated in (E), (F), and (I).

(C) Crystal structure of APC2 WHB domain bound to UBE2C (Brown et al., 2015), oriented as APC2 WHB-domain-BUBR1 interface in (B), shows how MCC in closed configuration blocks UBE2C binding.

(D) Close-up view of APC8 (A) TPR pocket shows density attributed to $CDC20_M$ IR tail, an interaction unique to the closed configuration of APC/C^{CDC20}-MCC.

(E) Mutating APC2-binding residues from BUBR1 substantially restores APC/C^{CDC20}Δ15-stimulated hydrolysis of oxyester-linked UBE2C~UB.

(legend continued on next page)

modification by APC/C^{CDC20}Δ15 that inhibited UBE2C-dependent priming of CDC20$_M$ (Figures 7E and S6C). Second, if a substrate is already marked by a UB, such as a UB-Securin* fusion, then the level of UBE2S-dependent chain growth would reflect that occurring upon MCC inhibition of D- and KEN-box access to CDC20$_A$, irrespective of whether APC/C^{CDC20}-MCC was closed or open. Indeed, the products of APC/C^{CDC20}-UBE2S-catalyzed ubiquitination reactions were similar with UB-Securin* in the presence of MCC or a different competitor (Hsl1) blocking the D- and KEN-box sites on CDC20$_A$ or in the absence of MCC but with a D- and KEN-box mutant UB-Securin* (Figures S6D and S6E). Thus, MCC competes with substrate binding, but, if an acceptor UB is accessible, UBE2S can elongate chains even with CDC20$_A$-MCC in the closed configuration (Figure 7F).

DISCUSSION

Overall, our data define conformational control and reciprocal regulation of APC/C^{CDC20} and MCC (Figure 7G). First, the cryo EM data reveal elements blocking degron motifs from accessing APC/C^{CDC20}-MCC, explaining how substrate ubiquitination is inhibited (Figures 3 and S3). Second, a range of CDC20$_A$-MCC orientations, coupled with conformational dynamics of the APC/C catalytic core, endows APC/C^{CDC20}-MCC with variable functions. Although targeting with UBE2C is blocked when APC/C^{CDC20}-MCC is closed, the open configuration places CDC20$_M$ ubiquitination sites (Lys485 and Lys490) for modification by activated UBE2C (Figure 4E). Since MCC does not impair UBE2S association (Kelly et al., 2014), polyubiquitination could occur rapidly in cells after CDC20$_M$ is initially primed by UBE2C (Figure 7E).

At this point, how APC/C^{CDC20}-MCC conformations are naturally toggled remains poorly understood. The strong stabilization of APC/C-MCC upon checkpoint activation in cells depleted of APC15 (Foster and Morgan, 2012; Mansfeld et al., 2011; Uzunova et al., 2012) raises the possibility that activating the checkpoint may involve shifting APC/C^{CDC20}-MCC to closed or down configurations. By contrast, mechanisms opening APC/C^{CDC20}-MCC would increase UBE2C∼UB activation and ubiquitination of CDC20$_M$, much like our mutations removing contacts unique to the closed conformation (Figure 6). It seems that UBE2C access is a crucial determinant controlling the reciprocal regulation of APC/C^{CDC20} and MCC. Indeed, UBE2C is a mediator of checkpoint silencing (Jia et al., 2011; Reddy et al., 2007; Varetti et al., 2011). UBE2C could potentially act as a wedge capturing APC/C^{CDC20}-MCC as it swings open. APC/C^{CDC20}-MCC conformation also could be influenced by factors affecting the APC4-APC5 region, which resembles a lever arm poised as a conduit between CDC20$_A$-MCC and the catalytic core (Figure S5E). This could potentially be regulated by several phosphorylation sites in APC5, which are substituted by glutamates in our recombinant APC/C^{CDC20} (Qiao et al., 2016).

BUB3 also regulates termination of the checkpoint (Vanoosthuyse et al., 2009; Windecker et al., 2009), but it is not visible in the EM maps (Figure 1). Interestingly, BUB3-mediated checkpoint silencing may involve binding to M-E-L-phosphoT sequences, and we note that such a sequence invisible in APC5 in the cryo-EM maps is potentially positioned to modulate APC/C^{CDC20}-MCC conformation (Vleugel et al., 2015; Yamagishi et al., 2012). The overall similarity of EM maps for APC/C^{CDC20}-MCC complexes with or without BUB3 also raises the question as to whether UBE2C could ubiquitinate CDC20 in the context of assembly/disassembly intermediates containing only subsets of MCC components (Eytan et al., 2013; Han et al., 2013).

It seems likely that the configurations of APC/C^{CDC20}-MCC mediating various roles (inhibition, CDC20$_M$ ubiquitination, or other functions such as MCC dissociation) rely on multisite interactions, where each element is weak on its own but synergistic formation or dismantling of multiple contacts governs conformational control of distinctive activities. Multisite regulation is emerging as a common mechanism controlling APC/C activities, including EMI1 inhibition of interphase APC/C^{CDH1} (Chang et al., 2015; Frye et al., 2013; Miller et al., 2006; Wang and Kirschner, 2013), and recruitment, positioning, and activation of APC/C's partner E2s to achieve different forms of ubiquitination (Brown et al., 2014, 2015, 2016; Chang et al., 2015; Kelly et al., 2014). Multisite interactions also can allow E3 regulators to straddle multiple functions (Figure S7). MCC represents a distinct manifestation of E3 modulator, as pan-inhibitor or selective substrate of APC/C^{CDC20} as needed (Figure 7G). It seems likely that there will be many other cases where subtle variations in regulation can determine when a single E3 regulator is an inhibitor, substrate, or modulator of UB ligation to establish dynamic cellular regulation.

EXPERIMENTAL PROCEDURES

Proteins and Assays

Proteins used in this study were human except for yeast Hsl1. Recombinant APC/C and its variants contain 100 phosphomimetic mutations (Qiao et al., 2016; Weissmann et al., 2016). CDC20, MCC, and variants were expressed in Hi5 insect cells, and then they were purified by nickel affinity, cation exchange, and size exclusion chromatography.

Substrate ubiquitination assays were performed as described, with MCC titrated from 15 to 250 nM (Brown et al., 2016; Qiao et al., 2016). CDC20 ubiquitination assays were adapted from Foe et al. (2011) and Foster and Morgan (2012) to use methyl UB, and they were extended to include UBE2S with WT UB. To distinguish CDC20 ubiquitination targets, CDC20$_A$ and CDC20$_M$ were N-terminally Myc- and FLAG-tagged, respectively, for two-color western

(F) Comparing APC/C^{CDC20}Δ15-stimulated activation of UBE2C∼UB in the presence of WT or BUBR1 mutant MCC, by quantification of UBE2C∼UB remaining after 3 hr from experiments as in (E), is shown. Error, SEM; n = 3.

(G) Mutating IR tail from CDC20$_M$ in MCC, but not a negative control region (C-box), substantially restores APC/C^{CDC20}Δ15-stimulated hydrolysis of oxyester-linked UBE2C∼UB.

(H) Quantification of UBE2C∼UB after 3 hr from experiments as in (G) is shown. Error. SEM; n = 3.

(I) Mutating APC2-binding residues from BUBR1 restores CDC20$_M$ ubiquitination by APC/C^{CDC20}Δ15 and UBE2C.

(J) Mutating CDC20$_M$ IR tail restores ubiquitination by APC/C^{CDC20}Δ15 and UBE2C.

See also Figure S5.

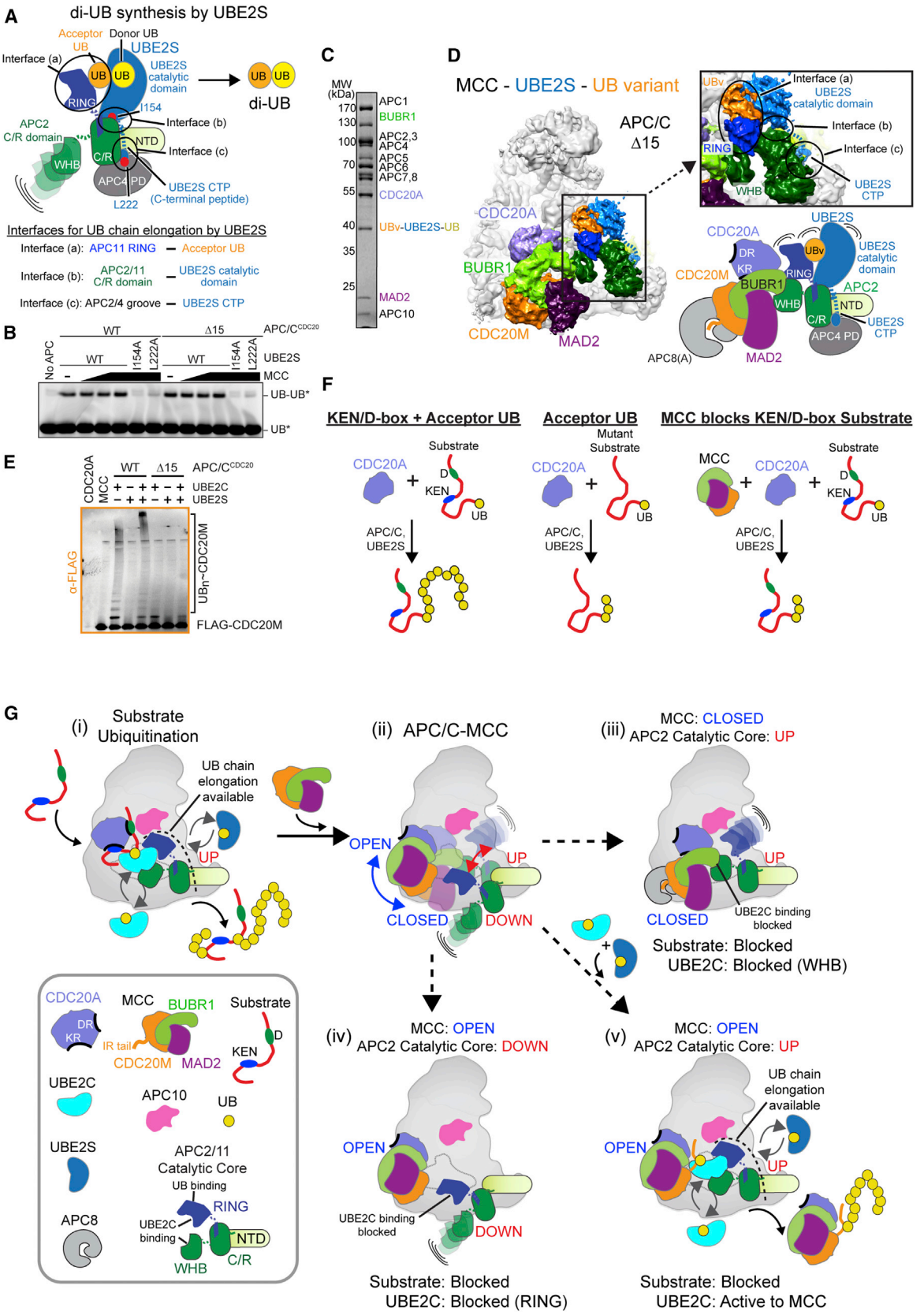

(legend on next page)

detection by secondary antibodies conjugated with DyLight 488 and Alexa 633, respectively, during a single scan with Typhoon FLA 9500.

Hydrolysis of oxyester-linked UBE2C∼UB (Brown et al., 2015) was performed three independent times, with 1 μM APC/C or APC/CΔ15, 1 μM CDC20, 5 μM UBE2C∼UB, and ±1 μM MCC at 30°C. Reaction products were visualized in Coomassie blue-stained 4%–12% NuPAGE gels (Life Technologies).

Complex Preparation for EM

Complexes were purified by sequential affinity pull-downs, followed by specific polishing steps. APC/C^{CDC20} and APC/C^{CDC20}-MCC, or versions lacking APC15, were prepared by either coexpressing APC/C, CDC20, and/or MCC or by mixing lysates from Hi5 insect cell cultures expressing components independently. Subcomplexes crosslinked to E2 active sites (UBE2C-substrate-UB [FLAG-tagged donor UB mimic], UBE2C-MCC [His$_6$-FLAG-tagged BUBR1], and UBE2S-UBv-UB [untagged]) were generated largely as described previously (Brown et al., 2015, 2016). Two- or three-way crosslinking between cysteine side chains was performed through the use of BMOE or TMEA (Pierce), respectively. Complexes were initially purified based on affinity tag(s) on APC/C, either a C-terminal Twin-Strep tag on APC4 or sequentially via an N-terminal Twin-Strep tag on APC2 and N-terminal GST tag on APC16. Complexes were enriched by FLAG affinity for BUBR1 or a donor UB mimic in some crosslinked complexes, with detailed purification procedures described in the Supplemental Experimental Procedures.

ACCESSION NUMBERS

The accession numbers for the data reported in this paper are Electron Microscopy Data Bank: EMD-4021, EMD-4022, EMD-4023, EMD-4024, EMD-4025, EMD-4026, EMD-4027, and EMD-4028 and Protein Data Bank: 5KHR and 5KHU.

SUPPLEMENTAL INFORMATION

Supplemental Information includes Supplemental Experimental Procedures, seven figures, three tables, and three movies and can be found with this article online at http://dx.doi.org/10.1016/j.molcel.2016.07.003.

AUTHOR CONTRIBUTIONS

M.Y., R.V., F.W., S.S.S., J.-M.P., H.S., and B.A.S. planned and supervised the project. M.Y., R.V., F.W., and R.Q. designed recombinant APC/C and MCC used herein. M.Y., R.V., N.G.B., and W.Z. performed biochemical analyses. M.Y., R.V., and N.G.B. made EM samples. P.D. and H.S. collected EM data, analyzed by M.Y., R.V., B.A.S., and H.S. with help from D.H. M.Y., R.V., J.-M.P., H.S., and B.A.S. prepared the paper.

ACKNOWLEDGMENTS

We thank M. Brunner, K.P. Wu, J.R. Michael, D.W. Miller, and S. Frase for advice and assistance. Funding was received from the Jane Coffin Childs Foundation, Leukemia & Lymphoma Society (N.G.B.); Austrian Science Fund FWF–Hertha Firnberg Program (R.Q.); Japan Society for the Promotion of Science (M.Y.); Canadian Institutes of Health Research (CIHR) MOP 111149 and 136956 (S.S.S.); Boehringer Ingelheim, the Austrian Science Fund (SFB-F34 and Wittgenstein award), the Austrian Research Promotion Agency (Headquarter grants FFG-832936 and FFG-852936 and Laura Bassi Centre for Optimized Structural Studies grant FFG-840283), and the European Community (FP7/2007-2013, grant 241548, MitoSys) (J.M.-P.); DFG Sonderforschungsbereich 860 (H.S.); and American Lebanese Syrian Associated Charities (ALSAC), NIH R37GM065930 and P30CA021765, and Howard Hughes Medical Institute (HHMI; B.A.S.).

Received: March 24, 2016
Revised: June 17, 2016
Accepted: July 7, 2016
Published: August 10, 2016

REFERENCES

Bolanos-Garcia, V.M., Lischetti, T., Matak-Vinković, D., Cota, E., Simpson, P.J., Chirgadze, D.Y., Spring, D.R., Robinson, C.V., Nilsson, J., and Blundell, T.L. (2011). Structure of a Blinkin-BUBR1 complex reveals an interaction crucial for kinetochore-mitotic checkpoint regulation via an unanticipated binding Site. Structure *19*, 1691–1700.

Braunstein, I., Miniowitz, S., Moshe, Y., and Hershko, A. (2007). Inhibitory factors associated with anaphase-promoting complex/cylosome in mitotic checkpoint. Proc. Natl. Acad. Sci. USA *104*, 4870–4875.

Brown, N.G., Watson, E.R., Weissmann, F., Jarvis, M.A., VanderLinden, R., Grace, C.R., Frye, J.J., Qiao, R., Dube, P., Petzold, G., et al. (2014). Mechanism of polyubiquitination by human anaphase-promoting complex: RING repurposing for ubiquitin chain assembly. Mol. Cell *56*, 246–260.

Brown, N.G., VanderLinden, R., Watson, E.R., Qiao, R., Grace, C.R., Yamaguchi, M., Weissmann, F., Frye, J.J., Dube, P., Ei Cho, S., et al. (2015). RING E3 mechanism for ubiquitin ligation to a disordered substrate visualized for human anaphase-promoting complex. Proc. Natl. Acad. Sci. USA *112*, 5272–5279.

Brown, N.G., VanderLinden, R., Watson, E.R., Weissmann, F., Ordureau, A., Wu, K.P., Zhang, W., Yu, S., Mercredi, P.Y., Harrison, J.S., et al. (2016). Dual RING E3 Architectures Regulate Multiubiquitination and Ubiquitin Chain Elongation by APC/C. Cell *165*, 1440–1453.

Figure 7. Multiple Catalytic and Conformational Mechanisms Contributing to Reciprocal Regulation of APC/C^{CDC20} and MCC

(A) Left: distinctive catalytic architecture for UBE2S-mediated diUB synthesis (Brown et al., 2016). Distinct surface of APC11 RING recruits acceptor UB. APC2 C/R domain activates UBE2S catalytic domain. APC2/APC4 (propeller domain [PD]) groove recruits UBE2S's unique C-terminal peptide (CTP). Key elements (APC11 RING UB-binding site, APC2-APC11 C/R domain, and APC2/APC4 groove) required for UB chain synthesis by UBE2S are available in the presence of MCC.

(B) Reactions with or without MCC monitoring WT or Δ15 APC/C^{CDC20} and UBE2S-catalyzed substrate-independent diUB* synthesis. UBE2S control mutants (I154A and L222A) confirm the role of catalytic architecture (Brown et al., 2014, 2016; Kelly et al., 2014).

(C) SDS-PAGE gel of purified APC/C^{CDC20}Δ15 complex with MCC core and three-way UBE2S-UBv-UB complex to represent UB chain elongation. UBv is a UB variant with enhanced affinity for the acceptor UB-binding surface of APC11 RING (Brown et al., 2016).

(D) Cryo-EM map shows complex from (C), representing overall conformational compatibility for UBE2S-dependent UB chain formation with APC/C^{CDC20}Δ15-MCC in the closed configuration.

(E) Experiment tests if UBE2S catalyzes UB chain elongation on MCC's CDC20$_M$ in the presence of UBE2C and either WT APC/C^{CDC20} or the mutant lacking APC15.

(F) Summary of (B)–(E) and Figures S6C and S6D. MCC inhibits D/KEN recruitment, but not intrinsic chain-forming activity of APC/C^{CDC20}-UBE2S, irrespective of APC15-dependent conformational modulation.

(G) Conformations of APC/C^{CDC20}-MCC determine reciprocal regulation. MCC degron-like elements mediate binding to CDC20$_A$ to inhibit substrate ubiquitination (i and ii). Rotation of the CDC20$_A$-MCC assembly and APC/C conformation determine if UBE2C is blocked from the APC2-APC11 catalytic core (iii and iv) or if CDC20 can be ubiquitinated by UBE2C (v). After an initial UB is linked, a UB chain can be extended by UBE2S.

See also Figures S6 and S7.

Burton, J.L., and Solomon, M.J. (2007). Mad3p, a pseudosubstrate inhibitor of APCCdc20 in the spindle assembly checkpoint. Genes Dev. *21*, 655–667.

Burton, J.L., Tsakraklides, V., and Solomon, M.J. (2005). Assembly of an APC-Cdh1-substrate complex is stimulated by engagement of a destruction box. Mol. Cell *18*, 533–542.

Chang, L., Zhang, Z., Yang, J., McLaughlin, S.H., and Barford, D. (2014). Molecular architecture and mechanism of the anaphase-promoting complex. Nature *513*, 388–393.

Chang, L., Zhang, Z., Yang, J., McLaughlin, S.H., and Barford, D. (2015). Atomic structure of the APC/C and its mechanism of protein ubiquitination. Nature *522*, 450–454.

Chao, W.C., Kulkarni, K., Zhang, Z., Kong, E.H., and Barford, D. (2012). Structure of the mitotic checkpoint complex. Nature *484*, 208–213.

Di Fiore, B., Davey, N.E., Hagting, A., Izawa, D., Mansfeld, J., Gibson, T.J., and Pines, J. (2015). The ABBA motif binds APC/C activators and is shared by APC/C substrates and regulators. Dev. Cell *32*, 358–372.

Diaz-Martinez, L.A., Tian, W., Li, B., Warrington, R., Jia, L., Brautigam, C.A., Luo, X., and Yu, H. (2015). The Cdc20-binding Phe box of the spindle checkpoint protein BubR1 maintains the mitotic checkpoint complex during mitosis. J. Biol. Chem. *290*, 2431–2443.

Eytan, E., Sitry-Shevah, D., Teichner, A., and Hershko, A. (2013). Roles of different pools of the mitotic checkpoint complex and the mechanisms of their disassembly. Proc. Natl. Acad. Sci. USA *110*, 10568–10573.

Foe, I.T., Foster, S.A., Cheung, S.K., DeLuca, S.Z., Morgan, D.O., and Toczyski, D.P. (2011). Ubiquitination of Cdc20 by the APC occurs through an intramolecular mechanism. Curr. Biol. *21*, 1870–1877.

Foley, E.A., and Kapoor, T.M. (2013). Microtubule attachment and spindle assembly checkpoint signalling at the kinetochore. Nat. Rev. Mol. Cell Biol. *14*, 25–37.

Foster, S.A., and Morgan, D.O. (2012). The APC/C subunit Mnd2/Apc15 promotes Cdc20 autoubiquitination and spindle assembly checkpoint inactivation. Mol. Cell *47*, 921–932.

Fraschini, R., Beretta, A., Sironi, L., Musacchio, A., Lucchini, G., and Piatti, S. (2001). Bub3 interaction with Mad2, Mad3 and Cdc20 is mediated by WD40 repeats and does not require intact kinetochores. EMBO J. *20*, 6648–6659.

Frye, J.J., Brown, N.G., Petzold, G., Watson, E.R., Grace, C.R., Nourse, A., Jarvis, M.A., Kriwacki, R.W., Peters, J.M., Stark, H., and Schulman, B.A. (2013). Electron microscopy structure of human APC/C(CDH1)-EMI1 reveals multimodal mechanism of E3 ligase shutdown. Nat. Struct. Mol. Biol. *20*, 827–835.

Fujimitsu, K., Grimaldi, M., and Yamano, H. (2016). Cyclin-dependent kinase 1-dependent activation of APC/C ubiquitin ligase. Science *352*, 1121–1124.

Garnett, M.J., Mansfeld, J., Godwin, C., Matsusaka, T., Wu, J., Russell, P., Pines, J., and Venkitaraman, A.R. (2009). UBE2S elongates ubiquitin chains on APC/C substrates to promote mitotic exit. Nat. Cell Biol. *11*, 1363–1369.

Ge, S., Skaar, J.R., and Pagano, M. (2009). APC/C- and Mad2-mediated degradation of Cdc20 during spindle checkpoint activation. Cell Cycle *8*, 167–171.

Han, J.S., Holland, A.J., Fachinetti, D., Kulukian, A., Cetin, B., and Cleveland, D.W. (2013). Catalytic assembly of the mitotic checkpoint inhibitor BubR1-Cdc20 by a Mad2-induced functional switch in Cdc20. Mol. Cell *51*, 92–104.

Hardwick, K.G., Johnston, R.C., Smith, D.L., and Murray, A.W. (2000). MAD3 encodes a novel component of the spindle checkpoint which interacts with Bub3p, Cdc20p, and Mad2p. J. Cell Biol. *148*, 871–882.

He, J., Chao, W.C., Zhang, Z., Yang, J., Cronin, N., and Barford, D. (2013). Insights into degron recognition by APC/C coactivators from the structure of an Acm1-Cdh1 complex. Mol. Cell *50*, 649–660.

Herzog, F., Primorac, I., Dube, P., Lenart, P., Sander, B., Mechtler, K., Stark, H., and Peters, J.M. (2009). Structure of the anaphase-promoting complex/cyclosome interacting with a mitotic checkpoint complex. Science *323*, 1477–1481.

Izawa, D., and Pines, J. (2015). The mitotic checkpoint complex binds a second CDC20 to inhibit active APC/C. Nature *517*, 631–634.

Jia, L., Li, B., Warrington, R.T., Hao, X., Wang, S., and Yu, H. (2011). Defining pathways of spindle checkpoint silencing: functional redundancy between Cdc20 ubiquitination and p31(comet). Mol. Biol. Cell *22*, 4227–4235.

Jia, L., Kim, S., and Yu, H. (2013). Tracking spindle checkpoint signals from kinetochores to APC/C. Trends Biochem. Sci. *38*, 302–311.

Kelly, A., Wickliffe, K.E., Song, L., Fedrigo, I., and Rape, M. (2014). Ubiquitin chain elongation requires E3-dependent tracking of the emerging conjugate. Mol. Cell *56*, 232–245.

Kim, S., and Yu, H. (2011). Mutual regulation between the spindle checkpoint and APC/C. Semin. Cell Dev. Biol. *22*, 551–558.

Kimata, Y., Baxter, J.E., Fry, A.M., and Yamano, H. (2008). A role for the Fizzy/Cdc20 family of proteins in activation of the APC/C distinct from substrate recruitment. Mol. Cell *32*, 576–583.

Kulukian, A., Han, J.S., and Cleveland, D.W. (2009). Unattached kinetochores catalyze production of an anaphase inhibitor that requires a Mad2 template to prime Cdc20 for BubR1 binding. Dev. Cell *16*, 105–117.

Lara-Gonzalez, P., Westhorpe, F.G., and Taylor, S.S. (2012). The spindle assembly checkpoint. Curr. Biol. *22*, R966–R980.

London, N., and Biggins, S. (2014). Signalling dynamics in the spindle checkpoint response. Nat. Rev. Mol. Cell Biol. *15*, 736–747.

Mansfeld, J., Collin, P., Collins, M.O., Choudhary, J.S., and Pines, J. (2011). APC15 drives the turnover of MCC-CDC20 to make the spindle assembly checkpoint responsive to kinetochore attachment. Nat. Cell Biol. *13*, 1234–1243.

Miller, J.J., Summers, M.K., Hansen, D.V., Nachury, M.V., Lehman, N.L., Loktev, A., and Jackson, P.K. (2006). Emi1 stably binds and inhibits the anaphase-promoting complex/cyclosome as a pseudosubstrate inhibitor. Genes Dev. *20*, 2410–2420.

Miniowitz-Shemtov, S., Teichner, A., Sitry-Shevah, D., and Hershko, A. (2010). ATP is required for the release of the anaphase-promoting complex/cyclosome from inhibition by the mitotic checkpoint. Proc. Natl. Acad. Sci. USA *107*, 5351–5356.

Musacchio, A. (2015). The molecular biology of spindle assembly checkpoint signaling dynamics. Curr. Biol. *25*, R1002–R1018.

Musacchio, A., and Ciliberto, A. (2012). The spindle-assembly checkpoint and the beauty of self-destruction. Nat. Struct. Mol. Biol. *19*, 1059–1061.

Nilsson, J., Yekezare, M., Minshull, J., and Pines, J. (2008). The APC/C maintains the spindle assembly checkpoint by targeting Cdc20 for destruction. Nat. Cell Biol. *10*, 1411–1420.

Pan, J., and Chen, R.H. (2004). Spindle checkpoint regulates Cdc20p stability in Saccharomyces cerevisiae. Genes Dev. *18*, 1439–1451.

Primorac, I., and Musacchio, A. (2013). Panta rhei: the APC/C at steady state. J. Cell Biol. *201*, 177–189.

Qiao, R., Weissmann, F., Yamaguchi, M., Brown, N.G., VanderLinden, R., Imre, R., Jarvis, M.A., Brunner, M.R., Davidson, I.F., Litos, G., et al. (2016). Mechanism of APC/CCDC20 activation by mitotic phosphorylation. Proc. Natl. Acad. Sci. USA *113*, E2570–E2578.

Reddy, S.K., Rape, M., Margansky, W.A., and Kirschner, M.W. (2007). Ubiquitination by the anaphase-promoting complex drives spindle checkpoint inactivation. Nature *446*, 921–925.

Sivakumar, S., and Gorbsky, G.J. (2015). Spatiotemporal regulation of the anaphase-promoting complex in mitosis. Nat. Rev. Mol. Cell Biol. *16*, 82–94.

Sudakin, V., Chan, G.K., and Yen, T.J. (2001). Checkpoint inhibition of the APC/C in HeLa cells is mediated by a complex of BUBR1, BUB3, CDC20, and MAD2. J. Cell Biol. *154*, 925–936.

Tian, W., Li, B., Warrington, R., Tomchick, D.R., Yu, H., and Luo, X. (2012). Structural analysis of human Cdc20 supports multisite degron recognition by APC/C. Proc. Natl. Acad. Sci. USA *109*, 18419–18424.

Uzunova, K., Dye, B.T., Schutz, H., Ladurner, R., Petzold, G., Toyoda, Y., Jarvis, M.A., Brown, N.G., Poser, I., Novatchkova, M., et al. (2012). APC15

mediates CDC20 autoubiquitylation by APC/C(MCC) and disassembly of the mitotic checkpoint complex. Nat. Struct. Mol. Biol. *19*, 1116–1123.

Van Voorhis, V.A., and Morgan, D.O. (2014). Activation of the APC/C ubiquitin ligase by enhanced E2 efficiency. Curr. Biol. *24*, 1556–1562.

Vanoosthuyse, V., Meadows, J.C., van der Sar, S.J., Millar, J.B., and Hardwick, K.G. (2009). Bub3p facilitates spindle checkpoint silencing in fission yeast. Mol. Biol. Cell *20*, 5096–5105.

Varetti, G., Guida, C., Santaguida, S., Chiroli, E., and Musacchio, A. (2011). Homeostatic control of mitotic arrest. Mol. Cell *44*, 710–720.

Vleugel, M., Omerzu, M., Groenewold, V., Hadders, M.A., Lens, S.M., and Kops, G.J. (2015). Sequential multisite phospho-regulation of KNL1-BUB3 interfaces at mitotic kinetochores. Mol. Cell *57*, 824–835.

Wang, W., and Kirschner, M.W. (2013). Emi1 preferentially inhibits ubiquitin chain elongation by the anaphase-promoting complex. Nat. Cell Biol. *15*, 797–806.

Weissmann, F., Petzold, G., VanderLinden, R., Huis In 't Veld, P.J., Brown, N.G., Lampert, F., Westermann, S., Stark, H., Schulman, B.A., and Peters, J.M. (2016). biGBac enables rapid gene assembly for the expression of large multisubunit protein complexes. Proc. Natl. Acad. Sci. USA *113*, E2564–E2569.

Wild, T., Larsen, M.S., Narita, T., Schou, J., Nilsson, J., and Choudhary, C. (2016). The spindle assembly checkpoint is not essential for viability of human cells with genetically lowered APC/C activity. Cell Rep. *14*, 1829–1840.

Williamson, A., Wickliffe, K.E., Mellone, B.G., Song, L., Karpen, G.H., and Rape, M. (2009). Identification of a physiological E2 module for the human anaphase-promoting complex. Proc. Natl. Acad. Sci. USA *106*, 18213–18218.

Windecker, H., Langegger, M., Heinrich, S., and Hauf, S. (2009). Bub1 and Bub3 promote the conversion from monopolar to bipolar chromosome attachment independently of shugoshin. EMBO Rep. *10*, 1022–1028.

Yamagishi, Y., Yang, C.H., Tanno, Y., and Watanabe, Y. (2012). MPS1/Mph1 phosphorylates the kinetochore protein KNL1/Spc7 to recruit SAC components. Nat. Cell Biol. *14*, 746–752.

Zhang, S., Chang, L., Alfieri, C., Zhang, Z., Yang, J., Maslen, S., Skehel, M., and Barford, D. (2016). Molecular mechanism of APC/C activation by mitotic phosphorylation. Nature *533*, 260–264.

Molecular Cell, Volume *63*

Supplemental Information

Cryo-EM of Mitotic Checkpoint Complex-Bound APC/C Reveals Reciprocal and Conformational Regulation of Ubiquitin Ligation

Masaya Yamaguchi, Ryan VanderLinden, Florian Weissmann, Renping Qiao, Prakash Dube, Nicholas G. Brown, David Haselbach, Wei Zhang, Sachdev S. Sidhu, Jan-Michael Peters, Holger Stark, and Brenda A. Schulman

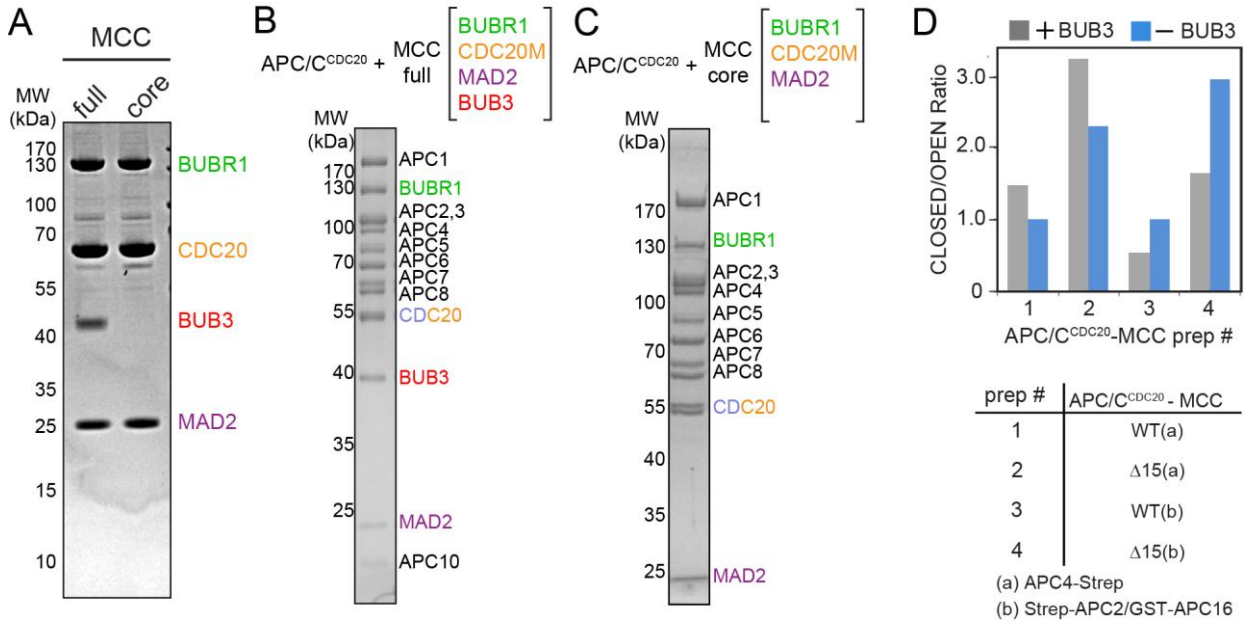

Figure S1. Common features of APC/C^{CDC20} complexes with MCC and the evolutionarily conserved MCC core (CDC20–MAD2–BUBR1) that lacks BUB3. Related to Figure 1.

(A-C) SDS-PAGE analysis of purified full MCC or the evolutionarily conserved core that lacks BUB3, alone or in complexes with APC/C^{CDC20}.
(D) To determine whether APC/C^{CDC20}–MCC core maintains the general conformational properties of APC/C^{CDC20}–MCC, or whether BUB3 plays a role, four matched pairs of APC/C^{CDC20} complexes with full or core MCC, with or without APC15 were prepared, analyzed by single particle negative stain EM, and 3D reconstructions were calculated. As described in Table S2, we tested two distinct affinity tag purification schemes (either APC4-Twin-Strep or double-affinity Twin-Strep-APC2/GST-APC16). The bar graph shows ratio of particles in 3D classes with CDC20$_A$–MCC in CLOSED over OPEN conformations. Excluding BUB3 had no consistent effect on the increased formation of CLOSED configurations in the absence of APC15.

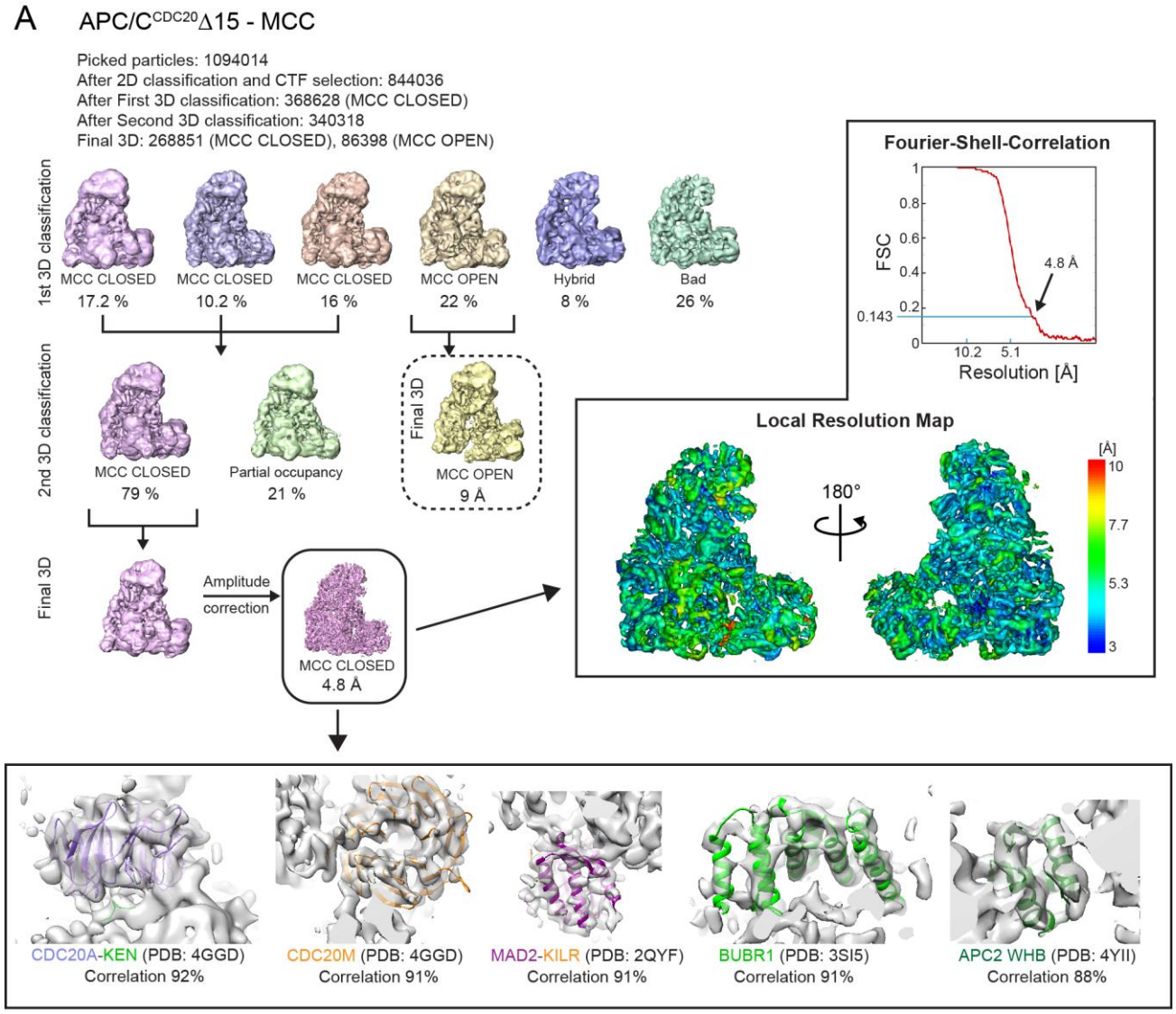
A
APC/C^CDC20Δ15 - MCC
Picked particles: 1094014
After 2D classification and CTF selection: 844036
After First 3D classification: 368628 (MCC CLOSED)
After Second 3D classification: 340318
Final 3D: 268851 (MCC CLOSED), 86398 (MCC OPEN)
1st 3D classification
MCC CLOSED 17.2 %
MCC CLOSED 10.2 %
MCC CLOSED 16 %
MCC OPEN 22 %
Hybrid 8 %
Bad 26 %
2nd 3D classification
MCC CLOSED 79 %
Partial occupancy 21 %
Final 3D
MCC OPEN 9 Å
Final 3D
Amplitude correction
MCC CLOSED 4.8 Å
Fourier-Shell-Correlation
FSC
4.8 Å
0.143
Resolution [Å]
Local Resolution Map
180°
[Å]
10
7.7
5.3
3
CDC20A-KEN (PDB: 4GGD) Correlation 92%
CDC20M (PDB: 4GGD) Correlation 91%
MAD2-KILR (PDB: 2QYF) Correlation 91%
BUBR1 (PDB: 3SI5) Correlation 91%
APC2 WHB (PDB: 4YII) Correlation 88%

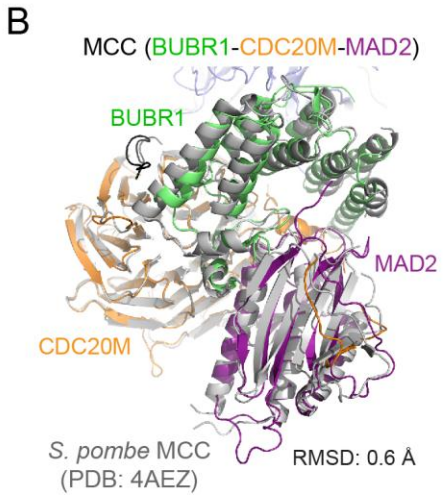
B
MCC (BUBR1-CDC20M-MAD2)
BUBR1
MAD2
CDC20M
S. pombe MCC (PDB: 4AEZ)
RMSD: 0.6 Å

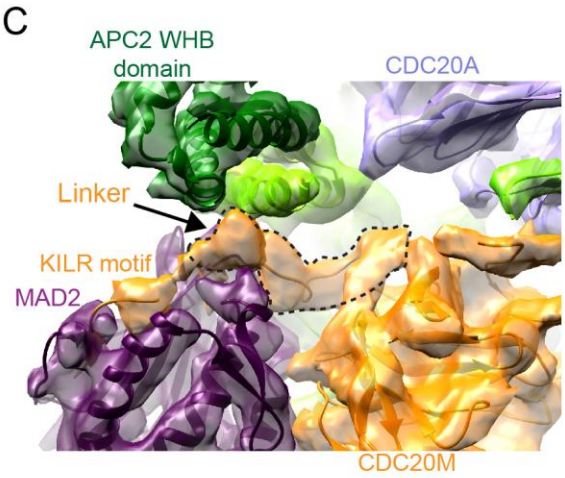
C
APC2 WHB domain
CDC20A
Linker
KILR motif
MAD2
CDC20M

Figure S2. Cryo EM reconstruction of APC/C^{CDC20}-MCC. Related to Figure 2.

(A) To obtain a cryo EM reconstruction for APC/C^{CDC20}Δ15-MCCcore, an initial 1,142,501 particle images were collected of which 67% were kept after 2D classification and particle sorting according to CTF parameters. After the first 3D classification, 42.4% of the particles divided in 3 subclasses displayed the CLOSED conformation for APC/C^{CDC20}Δ15-MCC, 1 class comprising 22% of the particles was OPEN, and the remaining 34% were classified as hybrid or bad. The 86,398 particles corresponding to APC/C^{CDC20}Δ15-MCC in the OPEN configuration were used to determine a final 3D structure to 9 Å, whereas those particles classified as corresponding to the CLOSED configuration were subjected to a second round of 3D classification. Ultimately, 268,851 particles in a subclass with full MCC occupancy were used for the final refinement to obtain a 3D structure at 4.8 Å resolution. The Gold-standard Fourier-Shell-Correlation ($FSC_{0.143}$) was used to determine the final overall resolution and we show opposing views of local resolution maps to demonstrate the resolution range. Crystal structures of human CDC20, BUBR1, and MAD2 were individually docked in the map using Chimera (Bolanos-Garcia et al., 2011; Tian et al., 2012; Yang et al., 2007), with additional elements generated by homology modeling and manual building in COOT (Emsley and Cowtan, 2004). A model for the human MCC core bound to APC/C^{CDC20}Δ15 was initially generated in Chimera (Pettersen et al., 2004), by fitting the high resolution structures of APC/C^{CDC20} lacking the APC4, APC5 and APC15 subunits (5G04.PDB) (Zhang et al., 2016), APC2's WHB domain that is invisible in APC/C^{CDC20} (4YII.PDB) (Brown et al., 2015), two copies of a CDC20-KEN-box complex (4GGD.PDB) (Tian et al., 2012) corresponding to $CDC20_A$–KEN2 and $CDC20_M$–KEN1, human BUBR1 (3SI5.PDB) (Bolanos-Garcia et al., 2011), and a human MAD2-peptide complex (2QYF.PDB) (Yang et al., 2007). Additional peptide segments were placed based on homology to other CDC20 or CDH1 complexes with D-boxes, KEN-boxes, or ABBA-motifs (He et al., 2013; Tian et al., 2012), or to BUBR1 homologs (Bolanos-Garcia et al., 2009; Chao et al., 2012; D'Arcy et al., 2010; Krenn et al., 2012). Because the APC4 lever-like helices/bundle are rotated relative to the propeller, APC4's propeller, helical and bundle domains were fit separately with the composite APC4 having a correlation to the map (4.8 Å) of 87% (Figure S5E). Residue changes, modeling into the peptide-like density for the pre-KEN region and CDC20 linker, deletion of residues in regions not visible in the map, joining the segments of APC4, and rigid body refinement were performed using COOT (Emsley and Cowtan, 2004).
(B) Model of human MCC core superimposed on the crystal structure of *S.pombe* MCC (4AEZ.PDB) (Chao et al., 2012).
(C) Density observed at the interface of BUBR1 and MAD2 was attributed to the linker between the KILR motif and β-propeller domain of $CDC20_M$.

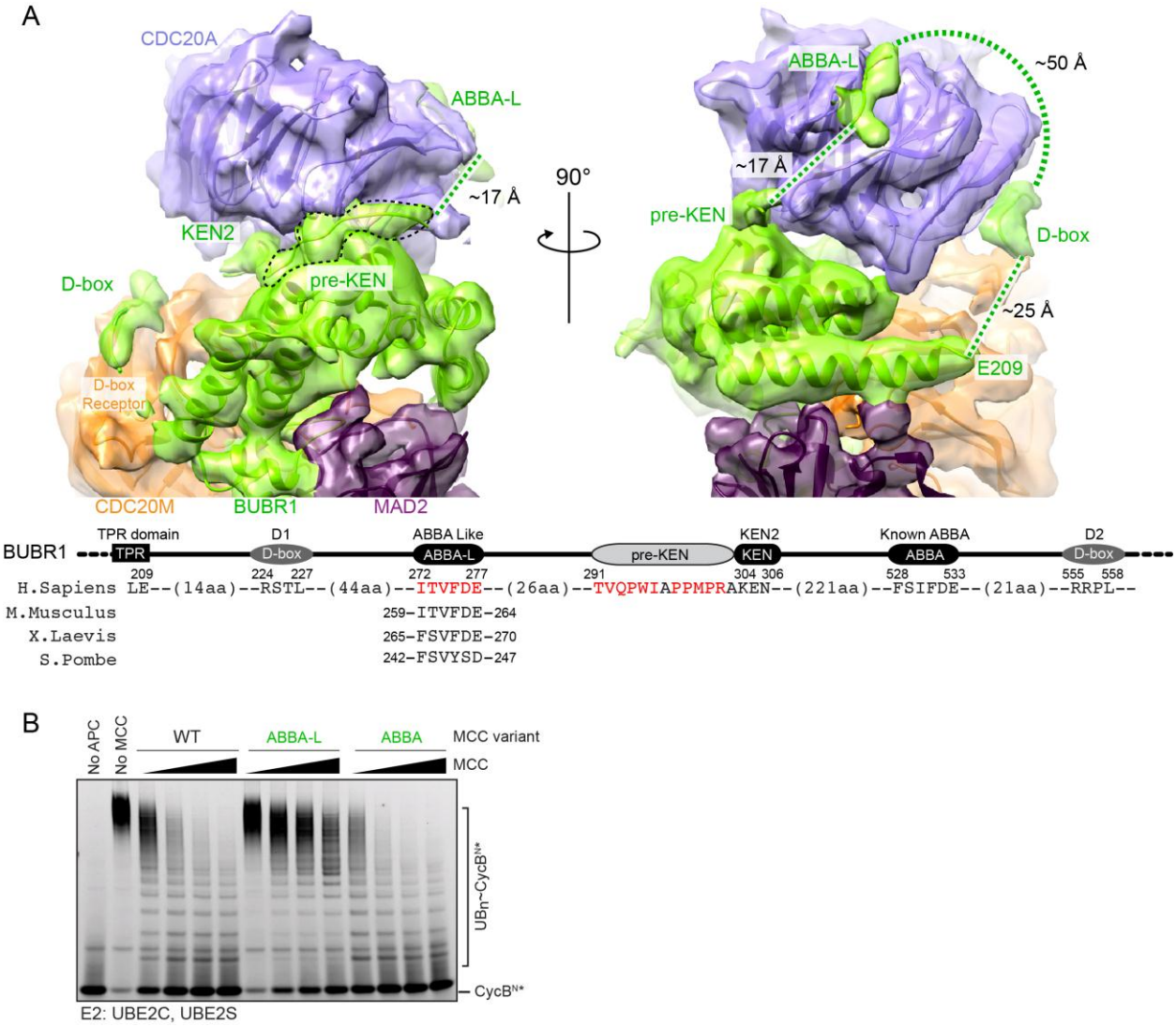

Figure S3. MCC elements mediating interactions with $CDC20_A$, as visualized in cryo EM reconstruction for APC/C^{CDC20}Δ15-MCC in CLOSED configuration. Related to Figure 3.

(A) EM reconstruction of APC/C^{CDC20}–MCC in CLOSED configuration showed density upstream of the pre-KEN/KEN peptide-like sequence resembling CDC20 interactions with an ABBA/Phe-box motif (Di Fiore et al., 2015; Diaz-Martinez et al., 2015; He et al., 2013; Lu et al., 2014). Due to sequence similarity of this region (ITVFDE) to an ABBA motif (e.g FSIFDE), we refer to this as ABBA-like (ABBA-L). The corresponding sequences of ABBA-L from *M.musculus*, *X. laevis* and *S. pombe* are shown below that of *H. sapiens* BUBR1.
(B) Assay testing effects of mutating BUBR1's ABBA-L and ABBA motif on MCC inhibition of substrate ubiquitination by APC/C^{CDC20}. Reaction products for APC/C^{CDC20}/UBE2C/UBE2S-dependent ubiquitination of the substrate $CycB^{N}$*, while titrating increasing concentrations of WT or BUBR1 ABBA-L (Ala substitutions for residues 272-277) or ABBA (Ala substitutions for residues 528-534) mutant MCC, were detected by fluorescent scan after SDS-PAGE.

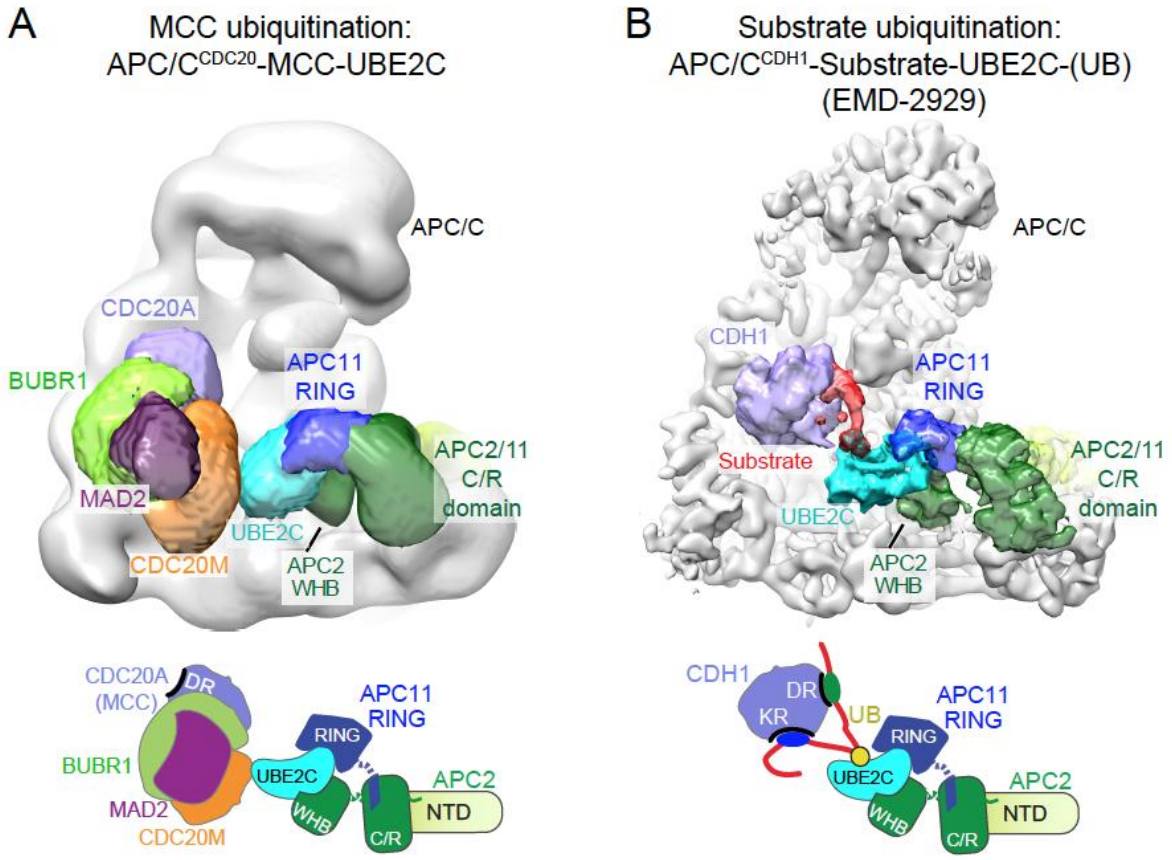

Figure S4. APC/C uses a common cullin-RING (APC2-APC11) structural mechanism to recruit, activate, and place UBE2C for ubiquitination of MCC's $CDC20_M$ or of a substrate. Related to Figure 4.
(A) Negative stain EM reconstruction of APC/C^{CDC20}–MCC–UBE2C with UBE2C's active site cross-linked to a preferred site of ubiquitination of $CDC20_M$ (residue 490, normally a Lys but here a Cys) prepared as in Figure 4D.
(B) Cryo EM reconstruction of an APC/C^{CDH1}–Substrate–UBE2C–UB complex, representing the architecture for substrate ubiquitination with UBE2C's active site cross-linked to a preferred site of ubiquitination from a peptide corresponding to the substrate Hsl1 (Brown et al., 2015). As described previously for the structural studies of substrate ubiquitination, the "donor" UB is not visible in the EM maps presumably due to conformational flexibility (Brown et al., 2015).

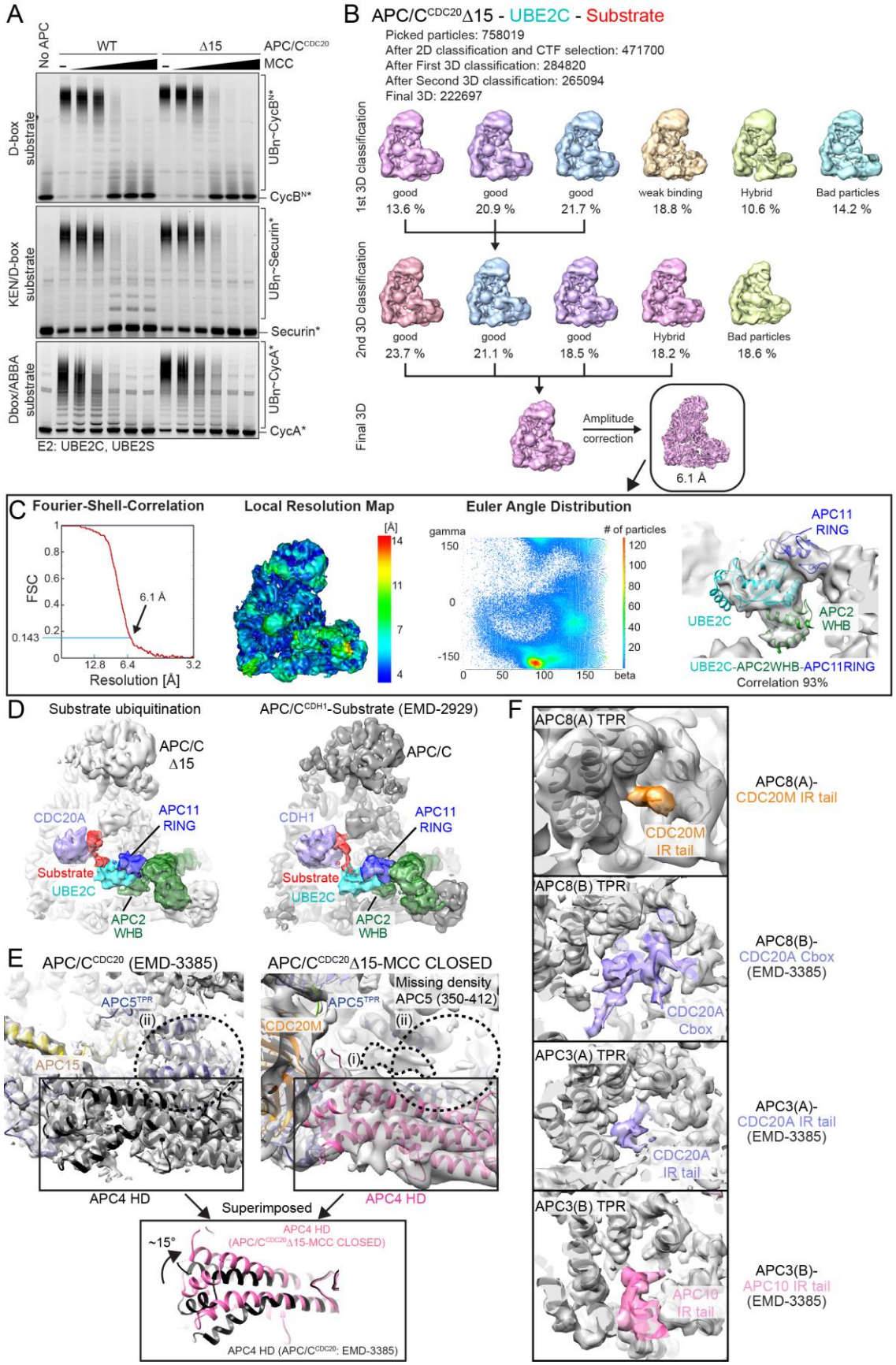
A
No APC
WT
Δ15
APC/C^CDC20
MCC
D-box substrate
KEN/D-box substrate
Dbox/ABBA substrate
UBn~CycB^N*
CycB^N*
UBn~Securin*
Securin*
UBn~CycA*
CycA*
E2: UBE2C, UBE2S
B
APC/C^CDC20Δ15 - UBE2C - Substrate
Picked particles: 758019
After 2D classification and CTF selection: 471700
After First 3D classification: 284820
After Second 3D classification: 265094
Final 3D: 222697
1st 3D classification
good 13.6 %
good 20.9 %
good 21.7 %
weak binding 18.8 %
Hybrid 10.6 %
Bad particles 14.2 %
2nd 3D classification
good 23.7 %
good 21.1 %
good 18.5 %
Hybrid 18.2 %
Bad particles 18.6 %
Final 3D
Amplitude correction
6.1 Å
C
Fourier-Shell-Correlation
FSC
0.143
6.1 Å
Resolution [Å]
Local Resolution Map
[Å]
Euler Angle Distribution
gamma
# of particles
beta
APC11 RING
UBE2C
APC2 WHB
UBE2C-APC2WHB-APC11RING
Correlation 93%
D
Substrate ubiquitination
APC/C^CDH1-Substrate (EMD-2929)
APC/C Δ15
CDC20A
APC11 RING
Substrate
UBE2C
APC2 WHB
APC/C
CDH1
E
APC/C^CDC20 (EMD-3385)
APC/C^CDC20Δ15-MCC CLOSED
APC5^TPR
(ii)
APC15
Missing density APC5 (350-412)
CDC20M
(i)
APC4 HD
Superimposed
~15°
APC4 HD (APC/C^CDC20Δ15-MCC CLOSED)
APC4 HD (APC/C^CDC20: EMD-3385)
F
APC8(A) TPR
CDC20M IR tail
APC8(A)-CDC20M IR tail
APC8(B) TPR
CDC20A Cbox
APC8(B)-CDC20A Cbox (EMD-3385)
APC3(A) TPR
CDC20A IR tail
APC3(A)-CDC20A IR tail (EMD-3385)
APC3(B) TPR
APC10 IR tail
APC3(B)-APC10 IR tail (EMD-3385)

Figure S5. Biochemical and structural characterization of APC/C^{CDC20}ΔAPC15. Related to Figure 5, 6.
(A) Assays monitoring MCC inhibition of ubiquitination of fluorescent substrates (CycB^{N}*, Securin*, or CycA*) by WT APC/C^{CDC20} or the mutant lacking the subunit APC15.
(B) The 3D reconstruction representing an APC/C^{CDC20}Δ15-UBE2C-UB-Substrate complex was determined in similar fashion to that described in Figure S2 for APC/C^{CDC20}Δ15-MCC in the CLOSED configuration. 758,019 particles were initially imaged and processed through particle sorting of 2D images and two rounds of 3D classification. Ultimately 222,697 particle images were used in the final refinement resulting in a 6.1 Å 3D structure.
(C) The Euler angle distribution, gold-standard Fourier-shell-correlation curve and local resolution map associated with these data are displayed. A model for APC/C^{CDC20}Δ15-UBE2C-substrate was generated in Chimera (Pettersen et al., 2004), by fitting the high resolution structures of APC/C^{CDC20} (5G04.PDB, without the APC15 subunit or APC11 RING domain; APC2 WHB domain is already absent in the coordinates) (Zhang et al., 2016), the crystal structure of a complex between APC2's WHB domain bound to UBE2C (4YII.PDB) and with APC11's RING domain docked on UBE2C as for the closely-related RBX1-E2 complex (Brown et al., 2015; Brown et al., 2014; Scott et al., 2014). As described previously for the EM reconstruction representing APC/C^{CDH1}-UBE2C-catalyzed substrate ubiquitination, the "donor" UB is not visible in the EM maps (Brown et al., 2015).
(D) Side-by-side comparison of EM reconstructions representing substrate ubiquitination with UBE2C. To the left is data for an APC/C^{CDC20}Δ15-UBE2C-substrate(-UB) complex, which superimposes well with the prior EM map of an APC/C^{CDH1}-UBE2C-substrate(-UB) complex (Brown et al., 2015). The "donor UB" is not visible in either map, potentially due to mobility (Pruneda et al., 2012), or due to our crosslinking method. This comparison shows that the removal of APC15 has little global effect on the potential for a coactivator-bound APC/C to recruit, activate, and place UBE2C.
(E) The EM density and models associated with the interface of APC4, APC5, and APC15 are shown for an APC/C^{CDC20}-substrate complex on the left (EMD-3385; 5G04.PDB) (Zhang et al., 2016), and APC/C^{CDC20}Δ15–MCC on the right. In comparison to WT complexes, EM maps for complexes lacking APC15 also lack clear density for three TPR helices from APC5 (residues 350-412), and instead there is evidence for a helix repacking in the TPR groove. The APC4 helical bundle domain, and the adjacent APC5 N-terminal domain contact an APC15 helix in WT APC/C, are relatively rotated in APC/C^{CDC20}Δ15–MCC in the CLOSED configuration (below). It seems that deleting APC15 influences the conformational malleability in this region in a manner that favors formation of the CLOSED configuration for APC/C^{CDC20}–MCC but does not obviously impact formation of the catalytic architecture for substrate ubiquitination.
(F) Comparison of IR tail/Cbox binding pockets in APC8/APC3. From top to bottom, APC8(A)-CDC20$_{M}$ IR tail as in Figure 6D, APC8(B)-CDC20$_{A}$ Cbox (EMD-3385), APC3(A)-CDC20$_{A}$ IR tail (EMD-3385), APC3(B)-APC10 IR tail (EMD-3385) (Zhang et al., 2016).

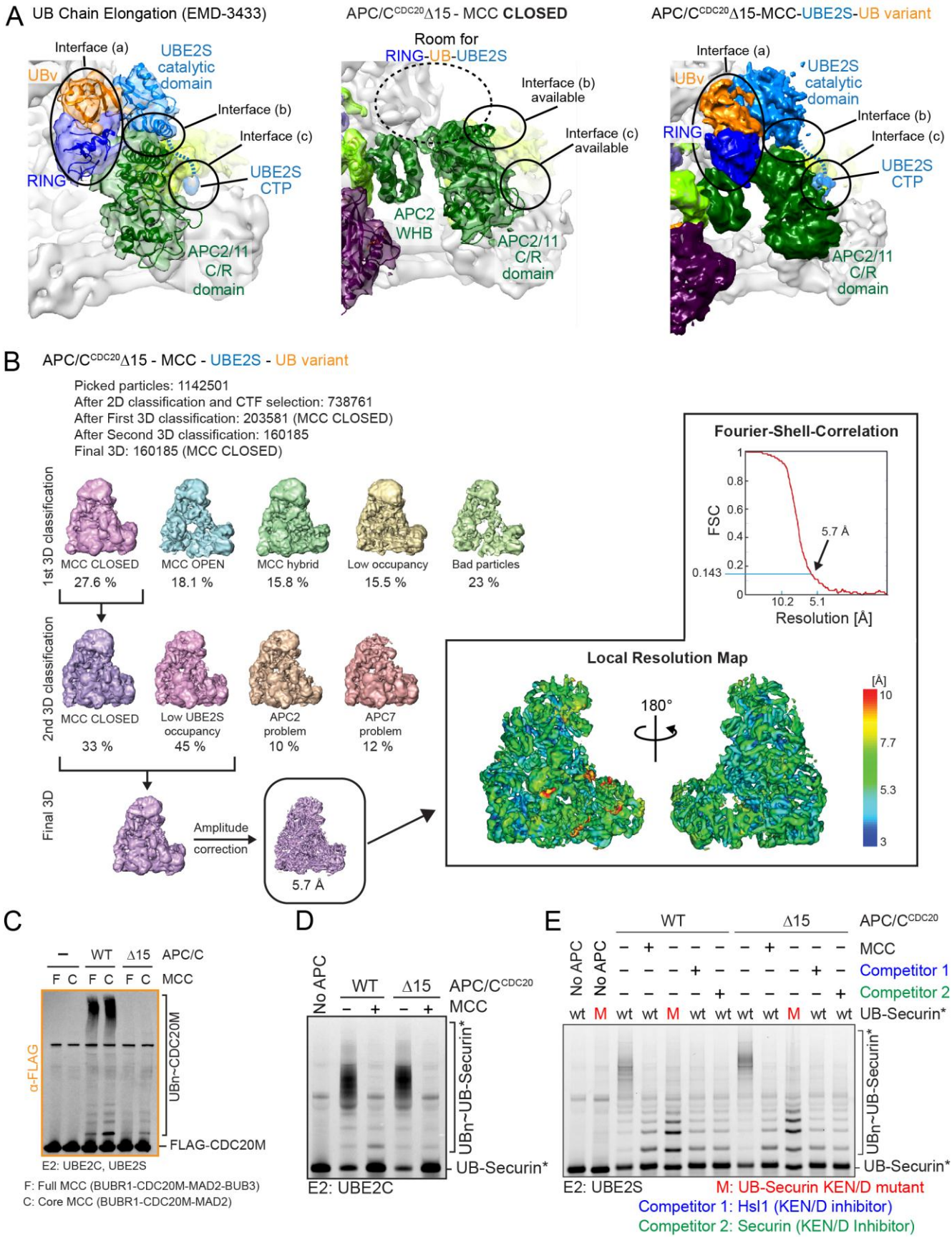
A
UB Chain Elongation (EMD-3433)
Interface (a)
UBE2S catalytic domain
UBv
Interface (b)
Interface (c)
RING
UBE2S CTP
APC2/11 C/R domain
APC/C^CDC20Δ15 - MCC CLOSED
Room for RING-UB-UBE2S
Interface (b) available
Interface (c) available
APC2 WHB
APC2/11 C/R domain
APC/C^CDC20Δ15-MCC-UBE2S-UB variant
Interface (a)
UBE2S catalytic domain
UBv
RING
Interface (b)
Interface (c)
UBE2S CTP
APC2/11 C/R domain
B
APC/C^CDC20Δ15 - MCC - UBE2S - UB variant
Picked particles: 1142501
After 2D classification and CTF selection: 738761
After First 3D classification: 203581 (MCC CLOSED)
After Second 3D classification: 160185
Final 3D: 160185 (MCC CLOSED)
1st 3D classification
MCC CLOSED 27.6 %
MCC OPEN 18.1 %
MCC hybrid 15.8 %
Low occupancy 15.5 %
Bad particles 23 %
2nd 3D classification
MCC CLOSED 33 %
Low UBE2S occupancy 45 %
APC2 problem 10 %
APC7 problem 12 %
Final 3D
Amplitude correction
5.7 Å
Fourier-Shell-Correlation
FSC
0.143
5.7 Å
Resolution [Å]
Local Resolution Map
180°
[Å]
10
7.7
5.3
3
C
– WT Δ15 APC/C
F C F C F C MCC
α-FLAG
UBn~CDC20M
FLAG-CDC20M
E2: UBE2C, UBE2S
F: Full MCC (BUBR1-CDC20M-MAD2-BUB3)
C: Core MCC (BUBR1-CDC20M-MAD2)
D
No APC
WT Δ15 APC/C^CDC20
– + – + MCC
UBn~UB-Securin*
UB-Securin*
E2: UBE2C
E
WT Δ15 APC/C^CDC20
No APC
No APC
MCC
Competitor 1
Competitor 2
wt M wt wt M wt wt wt wt M wt wt UB-Securin*
UBn~UB-Securin*
UB-Securin*
E2: UBE2S
M: UB-Securin KEN/D mutant
Competitor 1: Hsl1 (KEN/D inhibitor)
Competitor 2: Securin (KEN/D Inhibitor)

Figure S6. Structural and functional analysis of APC/C^{CDC20}–MCC activation of UBE2S-catalyzed UB chain synthesis in the presence or absence of APC15. Related to Figure 7.

(A) Side-by-side comparison of the published cryo EM reconstruction representing UBE2S poised for UB chain elongation on a UBv-fused substrate (Brown et al., 2016), of APC/C^{CDC20}Δ15-MCCcore, and of a complex between APC/C^{CDC20}Δ15-MCCcore and UBE2S with its active site cross-linked to the acceptor site (residue 11) on the UBv. The UBv (orange) is a mutant version of UB with enhanced affinity for the acceptor UB binding site on APC11's RING domain (dark blue) (Brown et al., 2016). UBE2S is shown in light blue, positioned by the previously-defined contacts to APC2 and APC4 (Brown et al., 2016). Key elements (APC11 RING's UB-binding site, APC2–APC11 C/R domain, and APC2/APC4 groove) required for UB chain synthesis by UBE2S are available in the presence of MCC.

(B) Determination of cryo EM reconstruction representing APC/C^{CDC20}Δ15-MCC, bound to UBE2S simultaneously cross-linked to a UB variant (UBv) and a donor UB mimic. This complex represents UB chain elongation by MCC-bound APC/C^{CDC20} and UBE2S. An initial 1,142,501 particles were picked of which 64.7% were kept after 2D classification and sorting. From the 1st 3D classification, 27.6% of the particles were classified with APC/C^{CDC20}Δ15-MCC in the CLOSED conformation. These particles were divided into four classes with 78% being intact APC/C-MCC particles but 45% having low occupancy of UBE2S, potentially due to a lack of anchoring without a substrate fused to the UBv (Brown et al., 2016), or due to a lack of specific enrichment for the crosslinked UBE2S-UBv-UB moiety during purification. The final three-dimensional reconstruction was computed with particles having both high and low UBE2S occupancy to a final resolution of 5.7 Å. The Gold-standard Fourier-Shell-Correlation was used to determine the resolution and we show opposing views of local resolution maps to demonstrate the resolution range.

(C) Experiment comparing full MCC and MCCcore for high molecular weight ubiquitin conjugate formation on $CDC20_M$ in the presence of UBE2S and UBE2C, with WT APC/C^{CDC20} or the mutant lacking APC15. There is no obvious impact of the presence or absence of BUB3 on $CDC20_M$ ubiquitination in this assay.

(D) Fluorescent scan of reactions testing if MCC inhibits ubiquitination of UB-Securin* by UBE2C and either WT APC/C^{CDC20} or the mutant lacking APC15. MCC concentration was 250 nM.

(E) UB chain elongation on fluorescent UB-Securin* by WT or Δ15 APC/C^{CDC20} and UBE2S. Inhibition by MCC was compared with WT activity toward KEN/D-box mutant UB-Securin* or inhibiting KEN/D-box-binding with excess cold Hsl1 or Securin.

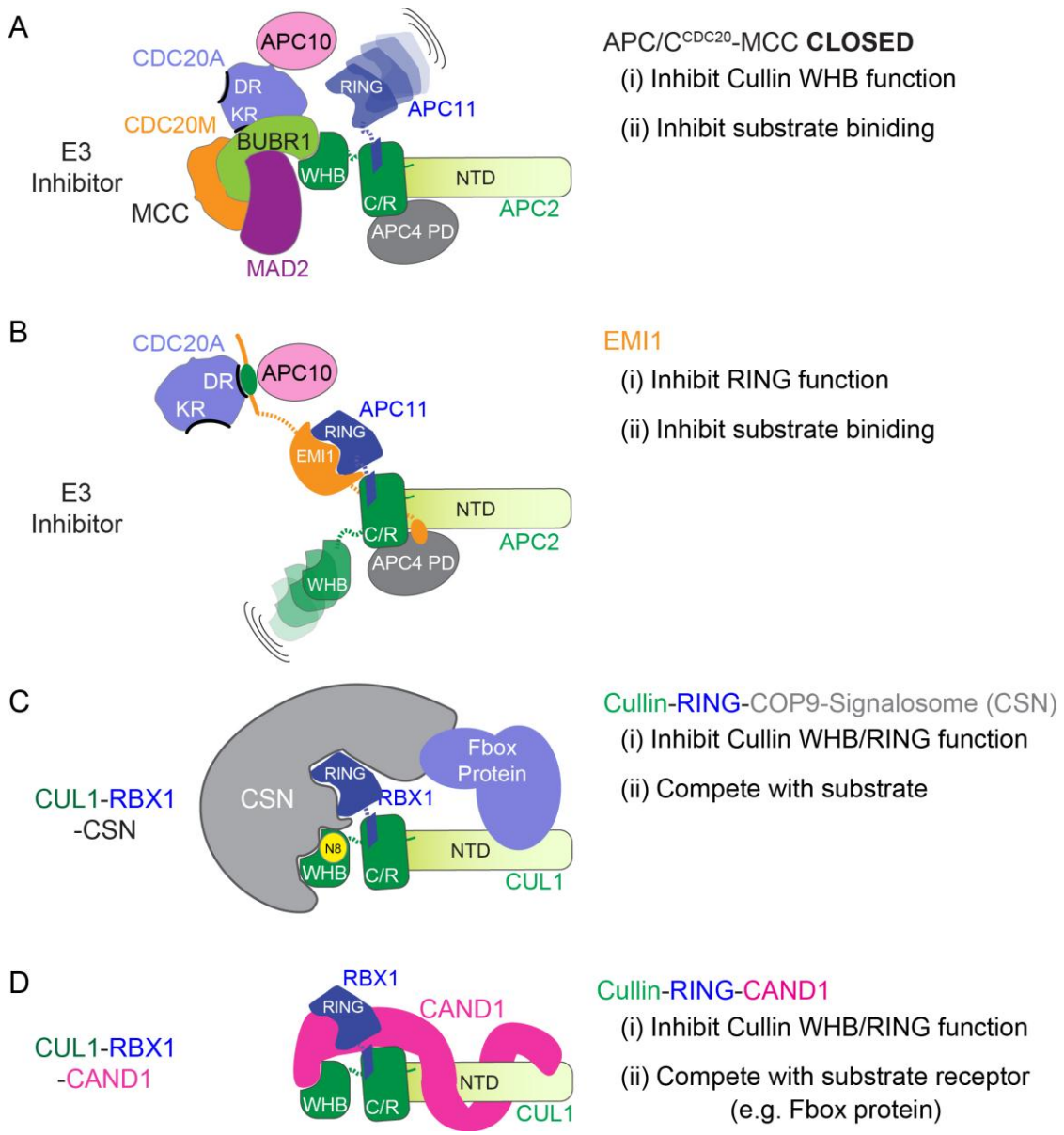

Figure S7. Multifunctional modulators of Cullin-RING Ligases. Related to Figure 7.

(A) MCC acts solely as an inhibitor when bound to APC/C^{CDC20} in the CLOSED configuration. This inhibits substrate binding to CDC20$_A$ via its key elements: D, KEN, ABBA-L, pre-KEN. In addition, MCC blocks UBE2C binding surface on APC2 WHB domain, inhibiting ubiquitination. However, conformational modulation, whereby APC/C^{CDC20}-MCC adopts an OPEN conformation allows CDC20$_M$ ubiquitination.
(B) During interphase, APC/C associates with a distinct coactivator CDH1, but binding to substrates, UBE2C and UBE2S are all blocked by EMI1 (Chang et al., 2015; Frye et al., 2013; Miller et al., 2006; Reimann et al., 2001; Wang and Kirschner, 2013).
(C, D) Classic "inhibitors" of cullin-RING ligases also depend on multisite binding and serve multiple functions. Perhaps the best-studied examples are the COP9 Signalosome (CSN, C) and CAND1 (D), which function in an intricate cycle involving dynamic protein-protein interactions and post-translational modifications to actually activate E3 ligase assembly, while likewise inhibiting post-translational modification of the cullin required for activity as indicated in the figure (Cavadini et al., 2016; Emberley et al., 2012; Enchev et al., 2012; Fischer et al., 2011; Goldenberg et al., 2004; Liu et al., 2002; Mosadeghi et al., 2016; Pierce et al., 2013; Siergiejuk et al., 2009; Wu et al., 2013; Zemla et al., 2013; Zheng et al., 2002).

Table S1. Statistics of EM reconstructions. Related to Figure 1-7.

Sample	EM Technique	Image frames	Particles in final 3D reconstruction	Resolution (Å)	Pixel size (Å)	EMDB / PDB Code	Figures
1) APC/C^{CDC20}-MCC **CLOSED**	CRYO	No	53143 (12.3%)	9	1.57	4023	1B, 1C, 2C
2) APC/C^{CDC20} – MCC **OPEN**	CRYO	No	57076 (13.2%)	10	1.57	4024	1B, 1C, 2D
3) APC/C^{CDC20}Δ15-MCC **CLOSED**	CRYO	Yes (17)	268851 (24.6%)	4.8	1.27	4021/ 5KHU	3B, 3C, 5D, 6B, 6D, S2A, S2C, S3A, S5E, S5F, S6A
4) APC/C^{CDC20}Δ15-MCC **OPEN**	CRYO	Yes (17)	86398 (7.9%)	9	1.27	4022	5E, 5F, S2A
5) APC/C^{CDC20}Δ15 - UBE2C-UB-substrate	CRYO	No	222697 (29.4%)	6.1	1.57	4025/ 5KHR	5C, S5B, S5C, S5D
6) APC/C^{CDC20}Δ15 – MCC - UBE2S-UBvariant-Ub	CRYO	Yes (17)	160,185 (14.0%)	5.7	1.57	4026	7D, S6A, S6B
7) APC/C^{CDC20}– MCC-UBE2C	NEGATIVE STAIN	No	(21.7%)	17	2.32	4027	4E, S4A
8) APC/C^{CDC20}Δ15– MCC - UBE2C	NEGATIVE STAIN	No	25472 (13%)	18	2.32	4028	6A
9) APC/C^{CDC20}– MCC **CLOSED**	NEGATIVE STAIN	No	9590 (5.4%)	20	2.5	NA	1D, 1E
10) APC/C^{CDC20}Δ15– MCC **OPEN**	NEGATIVE STAIN	No	15274 (8.6%)	20	2.5	NA	1D, 1E
11) APC/C^{CDC20}-MCCcore **CLOSED**	NEGATIVE STAIN	No	10548 (11.0%)	18	2.5	NA	1F, 1G
12) APC/C^{CDC20}-MCCcore **OPEN**	NEGATIVE STAIN	No	8726 (9.1%)	18	2.5	NA	1F, 1G

Table S2. APC/C^{CDC20}-MCC list of samples prepared for EM. Related to Figure 1, 5, 7.

		APC/C Affinity tags	CDC20	MCC	Purification Scheme	CLOSED/ OPEN Ratio
Cryo EM	***Fig. 1B***	APC4-Strep	WT	WT	1	ND
	Fig. 5D	APC4-Strep	WT	pE-core	2	ND
	Fig. 5C	Strep-APC2 /GST-APC16	WT	-	3	ND
	Fig. 7D	APC4-Strep	WT	pE-core	2	ND
Negative Stain EM (Fig. 5G, Fig. S1D)	***1 + APC15***	APC4-Strep	WT	WT	4	1.14
	1 - APC15					No OPEN
	2 + APC15 *	APC4-Strep	WT	pE	4	1.49
	2 - APC15 *					3.24
	3 + APC15 *	APC4-Strep	WT	pE-core	2	1.00
	3 - APC15 *					2.30
	4 + APC15 *	Strep-APC2 /GST-APC16	WT	pE	3	0.55
	4 - APC15 *					1.66
	5 + APC15 *	Strep-APC2 /GST-APC16	WT	pE-core	3	1.00
	5 - APC15 *					2.96
	6 + APC15	APC4-Strep	6A	WT	4	0.84
	6 - APC15					No OPEN
	7 + APC15	APC4-Strep	6A	pE-core	4	0.48
	7 - APC15					4.13

* CLOSED/OPEN ratio used in Figure S1D

Variants

6A: S41A, T55A, T59A, T69A, T70A, T106A in CDC20
pE: S41E, T70E, S92E, T106E, S368E in CDC20
and S367E, S435E, S543E, T600E, S665E, S670E, S720E, S1043E in BUBR1
core: No BUB3

Purification Scheme

1) APC/C-MCC coexpression > Strep Affinity > FLAG Affinity
2) APC/C-CDC20 colysis > Strep Affinity > Mix MCC > FLAG Affinity
3) APC/C-CDC20 colysis > Strep Affinity > GST Affinity > Mix MCC > FLAG Affinity
4) APC/C-CDC20 colysis > Strep Affinity > Anion Exchange > Size Exclusion > Mix MCC > FLAG Affinity

Table S3. Summary of APC2-APC11 catalytic core position (UP/DOWN) in APC/C-MCC sample. Related to Figure 5.

APC/C^{CDC20}-MCC prep	# of Samples	# of classes OPEN	OPEN/ UP	OPEN/ DOWN
WT	7	16	16	0
Δ15	13	14	1	13

Supplemental Movie S1. Dynamics between CLOSED and OPEN configurations of APC/C^{CDC20}-MCC shown by morphing cryo EM maps. See also Figure 1.

Supplemental Movie S2. Dynamics between CLOSED and OPEN configurations of APC/C^{CDC20}-MCC shown by morphing MCC model on superimposed cryo EM maps. See also Figure 1.

Supplemental Movie S3. Dynamics of the OPEN configuration of APC/C^{CDC20}-MCC shown by morphing negative stain EM maps. See also Figure 1.

Supplemental Experimental Procedures

Protein Purification.

For ubiquitination assays, human APC/C and its variants, UBA1, UBE2C and its variants, UBE2S, and donor UB were purified as described (Brown et al., 2015; Brown et al., 2014; Yamaguchi et al., 2015). APC/C in this study has 68 Ser and Thr residues that are sites of mitotic phosphorylation mutated to glutamates (Qiao et al., 2016). Because the APC/C contains two protomers of APC3, APC6, APC7, APC8, and CDC26/APC12, there are 100 total glutamate substitutions within the complex (Qiao et al., 2016). Unlabeled substrates Securin and Hsl1 (768-842) and labeled substrates, which were single cysteine versions of CyclinB^{N}* (residues 1-95), Securin* and acceptor UB*, were purified and fluorescently labeled, as denoted by an askterisk (*), with fluorescein-5 maleimide as described previously (Brown et al., 2015; Brown et al., 2014; Yamaguchi et al., 2015). CyclinA2 was expressed as a GST-TEV-GGGG-Strep- fusion protein in BL21 (DE3) Codon Plus (RIL) *Escherichia coli* cells and purified by GST affinity chromatography followed by affinity tag cleavage by TEV protease. The resultant GGGG-Strep-CyclinA2 was further purified by size exclusion chromatography (SEC). CyclinA2 was then fluorescently labeled by Sortase A (Dorr et al., 2014; Mao et al., 2004; Theile et al., 2013)mediated fusion of a fluorescein-5 maleimide containing Leu-Pro-Glu-Thr-Gly-Gly peptide and then further purified by Streptactin affinity chromatography and SEC. 3xMyc-HIS$_6$-CDC20 (Myc-CDC20$_A$) was expressed in High Five insect cells (Thermo Fisher Scientific), and purified by nickel affinity, cation exchange, and SEC. Specifically, cells were resuspended in buffer (20 mM HEPES, pH 7.0, 100 mM $(NH_4)_2SO4$, 2.5% glycerol, and 2mM DTT) and supplemented with protease inhibitors, lysed by sonication, and the cell lysate clarified by centrifugation (32,500xg, 60 min). Myc-CDC20$_A$ was extracted from the lysate with HIS-Select Nickel Affinity Gel (Sigma), washed with buffer and eluted with buffer supplemented with 250 mM Imidazole. Myc-CDC20$_A$ was then captured on SP sepharose (Sigma), washed with buffer supplemented with 100 mM NaCl and eluted with a gradient to 400 mM NaCl. Finally, Myc-CDC20$_A$ is put over a Superdex200 (GE Life Sciences) in 20 mM HEPES pH 7.0, 300 mM $(NH_4)_2SO4$, 2.5% glycerol, and 2mM DTT. MCC and its variants were also expressed in High Five insect cells with an N-terminal HIS$_6$-FLAG tag on BUBR1 and purified in a similar scheme as Myc-CDC20$_A$ with the following exceptions: buffer consisted of 20 mM HEPES, pH 7.5, 200 mM NaCl, 2 mM DTT, when necessary the affinity tag was cleaved by TEV protease during overnight dialysis (20 mM HEPES, pH 7.5, 100 mM NaCl, 2 mM DTT), MCC was eluted from SP sepharose with a gradient to 500 mM NaCl, and the final buffer for SEC was 20 mM HEPES pH 7.5, 200 mM NaCl, 2 mM DTT. Alternatively, MCC was also prepared by two-step affinity purification, in like buffers, via an N-terminal HIS$_6$ tag on BUBR1 and an N-terminal GST tag on MAD2 followed by SEC. The mutants used in this study are the following: KEN-box receptor (N329A/N331A/T377A/R445A), CRY-box (C165D/R166D/Y167A), K485R/K490R, and 6A (S41A/T55A/T59A/T69A/ T70A/ T106A), ΔCbox (Δ77-83), ΔCTR (Δ491-499), ΔIR (Δ498-499) for CDC20, and S201D/T204D, L205D/L208D, S201D/T204D/L205D/L208D, R169D/D172A/Q176A/Q197A/L205D/L208D, D1 (R224A/L227A), KEN2 (K304A/E305A/N306A), pre-KEN (T291A/V292A/Q293A/P294A/W295A/I296A/P298A/P299A/ M300A/P301A/R302A), ABBA-L (I272A/T273A/V274A/F275A/D276A/E277A), ABBA (F528A/S529A/I530A/F531A/D532A/E533A) for BUBR1 (Izawa and Pines, 2015; Labit et al., 2012; Reis et al., 2006; Tian et al., 2012).

Preparation of APC/C^{CDC20}-MCC for Electron Microscopy (EM)

Recombinant APC/C^{CDC20}-MCC for use in structural studies by EM was prepared by either coexpression of APC/C ^{CDC20}-MCC or mixing of purified components. For co-expression, High Five insect cells were co-infected with three baculoviruses containing all the subunits of APC/C and MCC including a Twin-Strep-tag on the C-terminus of APC4 and a HIS$_6$-FLAG tag on the N-terminus of BUBR1. Cell pellets were resuspended in lysis buffer (50 mM HEPES, pH 8.0, 250 mM NaCl, 5% glycerol, 2 mM DTT, 2 mM Benzamidine (Sigma), and 5 units/ml benzonase (Sigma), 10 µg/ml Leupeptin (Sigma), 20 µg/ml Aprotnin (Sigma), 1 EDTA-free protease inhibitor tablet per 50 mL (Roche)), lysed by sonication, and clarified by centrifugation at 32,500 xg. Purification of APC/C^{CDC20} or APC/C^{CDC20}-MCC from the clarified lysate was carried out by affinity purification on Strep-Tactin sepharose (IBA) and subsequent immunopurification on anti-DYKDDDDK G1 Affinity Resin (GenScript) following resin manufacturer protocols with a base buffer consisting of 50 mM HEPES, pH 8.0, 200 mM NaCl, 2.5% glycerol, 0.5 mM TCEP and 2 mM Benzamidine. 2.5 mM Desthiobiotin and 150 µg/ml FLAG peptide was added to the base buffer for elution from the Strep-Tactin sepharose and anti-DYKDDDDK G1 Affinity Resin, respectively.

For samples where purified components were combined, APC/C^{CDC20} was first prepared by co-lysing cells expressing APC/C or CDC20 followed by either a single affinity purification step via a C-terminal Twin-Strep-tag on APC4, dual affinity purification steps via N-terminal Twin-Strep-tag and GST tag on APC2 and APC16, respectively, or by the affinity purification, anion exchange, and SEC. The Strep affinity step was performed as

described above. For the GST affinity step, the Streptactin eluate was loaded directly on to equilibrated GS4B resin (GE Life Sciences), washed with base buffer and eluted with 20 mM reduced glutathione. The anion exchange and SEC steps were performed as described previously (Brown et al., 2015; Brown et al., 2014; Yamaguchi et al., 2015). Purified APC/C^{CDC20} was incubated with a substoichiometric amount of purified MCC or MCC-UBE2C, HRV14 3C protease to remove the affinity tags from APC/C, and anti-DYKDDDDK G1 Affinity Resin for one hour before washing the resin with base buffer and eluting with FLAG peptide. 110 ug of purified APC/C ^{CDC20}-MCC was loaded onto a GraFix gradient (Kastner et al., 2008), consisting of 10%–40% glycerol, 0.025%-0.1% gluteraldehyde, 50 mM HEPES pH 8.0, 200 mM NaCl, 2 mM MgCl2. Centrifugation was performed at 34,000 rpm in a SW55TI rotor (Beckman) for 15 hr at 4°C. The peak protein fraction of the gradient as determined by BioRad protein assay was used for EM studies.

Preparing complex representing APC/C^{CDC20}Δ15 with UBE2C active site targeting a substrate.

Our approach for trapping APC/C complexes with UBE2C active site targeting a substrate has been described (Brown et al., 2015; Brown et al., 2016). Briefly, UBE2C and target, with or without a UB representing a donor, are crosslinked based on our finding that combining several poor affinity interactors enables avidly capturing catalytically-relevant binding sites within APC/C. Toward this end, model substrates and targets are first identified biochemically, prior to designing peptide or protein targets. Here, the "substrate" was a peptide derived from the high affinity binding substrate yeast Hsl1, with the residue corresponding to the preferred ubiquitination site (normally Lys788) modified for crosslinking to a version of UBE2C harboring a single Cys at the active site. The cross-linked UBE2C-Substrate complex was prepared as previously described, with a FLAG-tagged donor UB mimic harboring a C-terminal Cys (Brown et al., 2015). Purified APC/C^{CDC20} was incubated with a substoichiometric amount of purified 3-way crosslinked UBE2C-Substrate-UB complex, with treated HRV14 3C protease to remove the affinity tags from APC/C, and purified by FLAG affinity chromatography. The APC/C^{CDC20}-UBE2C-Substrate complex was polished through GraFix for EM analysis as stated above.

Preparing APC/C^{CDC20}-MCC-UBE2C and APC/C^{CDC20}Δ15-MCC-UBE2C complexes.

The same protocol was used to generate complexes for WT APC/C^{CDC20} and the mutant expressed without APC15. The crosslinking strategy to generate a complex with UBE2C's active site affixed to a preferred target (normally Lys490 but here a Cys) was largely similar to that previously described (Brown et al., 2015; Kamadurai et al., 2013). First, a peptide (CDC20^{C}) was synthesized corresponding to 19-residues of CDC20's C-terminus, with the K490C substitution, and four N-terminal glycines (acetyl-GGGGKASAA"C"SSLIHQGIR-NH_2). A 2-way cross-linked complex was then formed between our single Cys version of UBE2C (C102A)-Strep and CDC20^{C} using the scheme illustrated in Figure 4D. Briefly, the proteins were treated with 10 mM DTT for 30 min before they were desalted into 50 mM HEPES 7.0, 400 mM NaCl. UBE2C was modified by addition 10 molar excess of BMOE (Thermo Fisher Scientific) for 15 min on ice. After removing unreacted BMOE by desalting, CDC20^{C}-UBE2C was prepared by reacting the CDC20^{C} with the UBE2C-BMOE at a 5:1 ratio for 1 hour at room temperature. The reaction was quenched with 10 mM β-mercaptoethanol and further purified by SEC. CDC20^{C}-UBE2C was then fused to the C-terminus of CDC20 in MCC by Sortase A mediated protein ligation as described (Dorr et al., 2014; Mao et al., 2004; Theile et al., 2013). In brief, MCC harboring CDC20 with a C-terminal LPETGG sequence at residue 476 (MCC^{LPETGG}), was expressed and purified as above. Then, 5 μM MCC^{LPETGG} and 20 μM CDC20^{C}-UBE2C were mixed at 4°C overnight with buffer containing 50 mM Tris pH 7.5, 150 mM NaCl, 10 mM $CaCl_2$ and 2 μM Sortase A. The resultant MCC-UBE2C complex was further purified by SEC and Strep affinity chromatography. Finally, MCC-UBE2C complex was mixed with purified APC/C^{CDC20} and APC/C^{CDC20}-MCC-UBE2C complex was immunoprecipitated based on an N-terminal FLAG tag on BUBR1, and polished through GraFix for EM analysis as described above for APC/C^{CDC20}-MCC alone.

Preparing APC/C^{CDC20}-MCC-UBE2S-UBv-UB complex.

Normally, UBE2S extends UB chains by catalyzing linkage of UB's Gly76 (donor) to Lys11 on an acceptor UB. Although UBE2S preferentially extends chains from UB-linked to D-/KEN- substrates at least in part due to their higher affinity and greater lifetime on APC/C^{CDC20}, intrinsic catalytic activity relies on specialized UBE2S recruitment to and activation by APC/C, as well as a distinct surface on APC11's RING domain reducing the K_m for the acceptor UB (Brown et al., 2014; Kelly et al., 2014). As such, APC/C^{CDC20} stimulates UBE2S-catalyzed linkage of UB to a free UB acceptor (di-UB synthesis) even in the absence of a substrate. Because structural analyses have been hampered by the extremely low affinity of an acceptor UB for APC11's RING domain, we previously used phage display to select a UB variant (UBv) with higher affinity for APC11's RING

domain, which when linked to a D-box peptide and cross-linked to the active site of UBE2S stabilized a complex representing UB chain elongation for structural studies (Brown et al., 2016).

Although MCC blocks binding to a KEN and/or D-box peptide, we considered that APC/C^{CDC20}Δ15 efficiently stimulated UBE2S-mediated di-UB synthesis in the presence of MCC (Figure 7B). To visualize this, we generated a trap with UBE2S's active site simultaneously 3-way cross-linked to residue 11 on the UBv and a Cys replacement for UB's C-terminus on a "donor" UB. Although the constructs used vary slightly, the same crosslinking strategy was used to generate cross-linked UBE2S-UBv-UB as that previously reported (Brown et al., 2016). APC/C^{CDC20}Δ15 was prepared by STREP affinity purification as described above, mixed with 2x molar excess purified MCC, incubated with HRV14 3C protease which removed affinity tags from APC4 of APC/C and then purified by SEC in 50 mM HEPES, pH 8.0, 200 mM NaCl, 2.5% glycerol, 0.5 mM TCEP. Peak fractions of the APC/CΔ15^{CDC20}-MCC complex were mixed in a 1:2 molar with UBE2S-UBv-UB and were further purified by immunoprecipitation using a FLAG tag on BUBR1 of MCC core, and by GraFix in a manner similar to that described above for APC/C^{CDC20}□□□□.

Enzyme Assays.

The qualitative APC/C-mediated ubiquitination assays were largely performed as previously described except for using 500 nM UBE2C and UBE2S, 150 nM CDC20, 90 nM fluorescently labeled (CycB^{N}*, Securin* and CycA*) plus the addition of MCC at 15, 30, 60, 120 and 250 nM (Brown et al., 2015; Yamaguchi et al., 2015). 15-250 nM of MCC was used in Figure 1A, 3E, 5B, 7B, S5A. 30-250 nM of MCC was used in Figure 3D, S3B.The ubiquitination of UB-Securin* was monitored in the presence of 250 nM MCC, 1000 nM free Hsl1 or 1000 nM free Securin. Each APC/C-mediated substrate ubiquitination experiment was subjected to SDS-PAGE and resulting gels were imaged with a Typhoon FLA 9500.

CDC20 ubiquitination assays were developed from the previously described assay using methylated UB to probe yeast Cdc20 ubiquitination (Foe et al., 2011; Foster and Morgan, 2012). 90 nM APC/C, 150 nM Myc-CDC20$_A$ and 250 nM MCC harboring FLAG-CDC20$_M$, and 90 nM CycB^{N}* when specified were incubated at 30°C with a mixture containing 100 nM E1, 500 nM UBE2C and/or UBE2S, 5 mM Mg/ATP and 150 μM UB or methylated UB. The MCC concentration was chosen based on the saturation of inhibition in substrate ubiquitination experiments. Reactions were quenched with SDS containing buffer at 2.5 min and 15 min for UB and methylated UB, respectively. The products of ubiquitination were analyzed by western blot. Specifically, Myc-CDC20$_A$ and Myc-CDC20$_A$~UBn products were detected by α-cMyc antibodies (sc-789, Santa Cruz) and α-rabbit IgG conjugated with DyLight 488 (Thermo Fisher Scientific) and FLAG-CDC20$_M$ and FLAG-CDC20$_M$~UBn products were detected by α-FLAG antibodies (F1804, SIGMA) and α-mouse IgG conjugated with Alexa Fluor 633 (Thermo Fisher Scientific). Western blot membranes were imaged with a Typhoon FLA 9500.

Western blot to confirm the absence of APC15 in recombinant APC/CΔ15.

The absence of APC15 in purified APC/CΔ15 was validated by western blot detecting APC3, APC10 and APC15 with α-APC3 (sc-9972, Santa Cruz), α-APC10 (sc-20989, Santa Cruz) and α-APC15 (sc-398488, Santa Cruz) antibodies, respectively.

Negative stain electron microscopy

Purified complexes were adsorbed to a thin film of carbon and then transferred to an electron microscopy grid covered with a perforated carbon film. The bound APC/C particles were stained with 2% (w/v) uranyl formate, blotted and air-dried for ~1 min at room temperature. Images were recorded at a magnification of 120,560× or 157,550× on a 4k × 4k CCD camera (TVIPS GmbH) using two-fold pixel binning (2.32 Å or 1.78 Å per pixel) in a Philips CM200 FEG electron microscope (Philips/FEI) operated at an acceleration voltage of 160 kV. At least 1000 images were recorded per dataset, particles were picked as described (Frye et al., 2013), and 3D classification was performed using RELION 1.3 (Scheres, 2012).

Cryo-electron microscopy

For cryo-EM, the GraFix fraction containing the desired complex was subjected to a buffer exchange procedure using Zeba spin columns (Pierce) to remove the glycerol prior to EM grid preparation. APC/C particles were allowed to adsorb on a thin film of carbon for 2 min, transferred onto a cryo-EM grid (Quantifoil 3.5/1, Jena) and then plunged into liquid ethane under controlled environmental conditions of 4 °C and 100% humidity in a vitrification device (Vitrobot Mark IV, FEI Company, Eindhoven). Images were recorded at low temperature on a Falcon II direct detector with a Titan Krios electron microscope (FEI, Eindhoven) equipped with an XFEG electron source and a Cs corrector (CEOS, Heidelberg) using 300 kV acceleration voltage. An electron dose of ~40 electrons

per $Å^2$, −0.7 to −3.5 μm defocus and a nominal magnification of 94,000× were used, resulting in a final calibrated pixel size of ~1.57 Å. CTF correction was performed by CTFFIND (Rohou and Grigorieff, 2015 JSB). Initial 2D sorting of images was performed based on CTF parameters. Only images showing isotropic Thon rings better than 6 Å were used for further processing. Additional image sorting was performed by applying several rounds of multivariate statistics, first without alignment and subsequently after image alignment to remove ice contaminations and bad particle images. The remaining good particle images were used for further processing. 3D classification in RELION 1.3 was used to obtain the particles revealing the highest MCC factor occupancy (Scheres, 2012). The best class was then used for the final refinement using the 'gold- standard procedure' in RELION 1.3. The final resolution was calculated by the Fourier-shell-correlation using the FSC 0.143 criterion and applying a soft mask with 7 voxel drop-off.

*Structure analysis***.**

Structural modeling is described in Figure S2A and Figure S5C.

In Figure 5G, S1D and Table S2, the ratio of APC/C^{CDC20}-MCC CLOSED over OPEN was determined by dividing the percent of particles in negative stain EM structural classes that adopt the CLOSED conformation by the percent of particles in structural classes that adopt OPEN conformations.

In Figure 5H and Table S3, the number of classes that represent OPEN/UP and OPEN/DOWN was determined.

Pymol and Chimera were used to generate figures of structures and EM densities (Pettersen et al., 2004; Schrodinger, 2010).

Supplemental References

Bolanos-Garcia, V.M., Kiyomitsu, T., D'Arcy, S., Chirgadze, D.Y., Grossmann, J.G., Matak-Vinkovic, D., Venkitaraman, A.R., Yanagida, M., Robinson, C.V., and Blundell, T.L. (2009). The crystal structure of the N-terminal region of BUB1 provides insight into the mechanism of BUB1 recruitment to kinetochores. Structure *17*, 105-116.

Bolanos-Garcia, V.M., Lischetti, T., Matak-Vinkovic, D., Cota, E., Simpson, P.J., Chirgadze, D.Y., Spring, D.R., Robinson, C.V., Nilsson, J., and Blundell, T.L. (2011). Structure of a Blinkin-BUBR1 complex reveals an interaction crucial for kinetochore-mitotic checkpoint regulation via an unanticipated binding Site. Structure *19*, 1691-1700.

Brown, N.G., VanderLinden, R., Watson, E.R., Qiao, R., Grace, C.R., Yamaguchi, M., Weissmann, F., Frye, J.J., Dube, P., Ei Cho, S., *et al.* (2015). RING E3 mechanism for ubiquitin ligation to a disordered substrate visualized for human anaphase-promoting complex. Proceedings of the National Academy of Sciences of the United States of America *112*, 5272-5279.

Brown, N.G., VanderLinden, R., Watson, E.R., Weissmann, F., Ordureau, A., Wu, K.P., Zhang, W., Yu, S., Mercredi, P.Y., Harrison, J.S., *et al.* (2016). Dual RING E3 Architectures Regulate Multiubiquitination and Ubiquitin Chain Elongation by APC/C. Cell *165*, 1440-1453.

Brown, N.G., Watson, E.R., Weissmann, F., Jarvis, M.A., VanderLinden, R., Grace, C.R., Frye, J.J., Qiao, R., Dube, P., Petzold, G., *et al.* (2014). Mechanism of polyubiquitination by human anaphase-promoting complex: RING repurposing for ubiquitin chain assembly. Molecular cell *56*, 246-260.

Cavadini, S., Fischer, E.S., Bunker, R.D., Potenza, A., Lingaraju, G.M., Goldie, K.N., Mohamed, W.I., Faty, M., Petzold, G., Beckwith, R.E., *et al.* (2016). Cullin-RING ubiquitin E3 ligase regulation by the COP9 signalosome. Nature *531*, 598-603.

Chao, W.C., Kulkarni, K., Zhang, Z., Kong, E.H., and Barford, D. (2012). Structure of the mitotic checkpoint complex. Nature *484*, 208-213.

D'Arcy, S., Davies, O.R., Blundell, T.L., and Bolanos-Garcia, V.M. (2010). Defining the molecular basis of BubR1 kinetochore interactions and APC/C-CDC20 inhibition. The Journal of biological chemistry *285*, 14764-14776.

Di Fiore, B., Davey, N.E., Hagting, A., Izawa, D., Mansfeld, J., Gibson, T.J., and Pines, J. (2015). The ABBA Motif Binds APC/C Activators and Is Shared by APC/C Substrates and Regulators. Developmental cell *32*, 358-372.

Diaz-Martinez, L.A., Tian, W., Li, B., Warrington, R., Jia, L., Brautigam, C.A., Luo, X., and Yu, H. (2015). The Cdc20-binding Phe box of the spindle checkpoint protein BubR1 maintains the mitotic checkpoint complex during mitosis. The Journal of biological chemistry *290*, 2431-2443.

Dorr, B.M., Ham, H.O., An, C., Chaikof, E.L., and Liu, D.R. (2014). Reprogramming the specificity of sortase enzymes. Proceedings of the National Academy of Sciences of the United States of America *111*, 13343-13348.

Emberley, E.D., Mosadeghi, R., and Deshaies, R.J. (2012). Deconjugation of Nedd8 from Cul1 is directly regulated by Skp1-F-box and substrate, and the COP9 signalosome inhibits deneddylated SCF by a noncatalytic mechanism. The Journal of biological chemistry *287*, 29679-29689.

Emsley, P., and Cowtan, K. (2004). Coot: model-building tools for molecular graphics. Acta crystallographica *60*, 2126-2132.

Enchev, R.I., Scott, D.C., da Fonseca, P.C., Schreiber, A., Monda, J.K., Schulman, B.A., Peter, M., and Morris, E.P. (2012). Structural basis for a reciprocal regulation between SCF and CSN. Cell reports *2*, 616-627.

Fischer, E.S., Scrima, A., Bohm, K., Matsumoto, S., Lingaraju, G.M., Faty, M., Yasuda, T., Cavadini, S., Wakasugi, M., Hanaoka, F., *et al.* (2011). The molecular basis of CRL4DDB2/CSA ubiquitin ligase architecture, targeting, and activation. Cell *147*, 1024-1039.

Foe, I.T., Foster, S.A., Cheung, S.K., DeLuca, S.Z., Morgan, D.O., and Toczyski, D.P. (2011). Ubiquitination of Cdc20 by the APC occurs through an intramolecular mechanism. Curr Biol *21*, 1870-1877.

Foster, S.A., and Morgan, D.O. (2012). The APC/C subunit Mnd2/Apc15 promotes Cdc20 autoubiquitination and spindle assembly checkpoint inactivation. Molecular cell *47*, 921-932.

Frye, J.J., Brown, N.G., Petzold, G., Watson, E.R., Grace, C.R., Nourse, A., Jarvis, M.A., Kriwacki, R.W., Peters, J.M., Stark, H., *et al.* (2013). Electron microscopy structure of human APC/C(CDH1)-EMI1 reveals multimodal mechanism of E3 ligase shutdown. Nature structural & molecular biology *20*, 827-835.

Goldenberg, S.J., Cascio, T.C., Shumway, S.D., Garbutt, K.C., Liu, J., Xiong, Y., and Zheng, N. (2004). Structure of the Cand1-Cul1-Roc1 complex reveals regulatory mechanisms for the assembly of the multisubunit cullin-dependent ubiquitin ligases. Cell *119*, 517-528.

He, J., Chao, W.C., Zhang, Z., Yang, J., Cronin, N., and Barford, D. (2013). Insights into degron recognition by APC/C coactivators from the structure of an Acm1-Cdh1 complex. Molecular cell *50*, 649-660.

Izawa, D., and Pines, J. (2015). The mitotic checkpoint complex binds a second CDC20 to inhibit active APC/C. Nature *517*, 631-634.

Kamadurai, H.B., Qiu, Y., Deng, A., Harrison, J.S., Macdonald, C., Actis, M., Rodgrigues, P., Miller, D.J., Souphron, J., Lewis, S.M., *et al.* (2013). Mechanism of ubiquitin ligation and lysine prioritization by a HECT E3. eLIFE *2*, e00828.

Kastner, B., Fischer, N., Golas, M.M., Sander, B., Dube, P., Boehringer, D., Hartmuth, K., Deckert, J., Hauer, F., Wolf, E., *et al.* (2008). GraFix: sample preparation for single-particle electron cryomicroscopy. Nat Methods *5*, 53-55.

Kelly, A., Wickliffe, K.E., Song, L., Fedrigo, I., and Rape, M. (2014). Ubiquitin chain elongation requires E3-dependent tracking of the emerging conjugate. Molecular cell *56*, 232-245.

Krenn, V., Wehenkel, A., Li, X., Santaguida, S., and Musacchio, A. (2012). Structural analysis reveals features of the spindle checkpoint kinase Bub1-kinetochore subunit Knl1 interaction. The Journal of cell biology *196*, 451-467.

Labit, H., Fujimitsu, K., Bayin, N.S., Takaki, T., Gannon, J., and Yamano, H. (2012). Dephosphorylation of Cdc20 is required for its C-box-dependent activation of the APC/C. The EMBO journal *31*, 3351-3362.

Liu, J., Furukawa, M., Matsumoto, T., and Xiong, Y. (2002). NEDD8 modification of CUL1 dissociates p120(CAND1), an inhibitor of CUL1-SKP1 binding and SCF ligases. Molecular cell *10*, 1511-1518.

Lu, D., Hsiao, J.Y., Davey, N.E., Van Voorhis, V.A., Foster, S.A., Tang, C., and Morgan, D.O. (2014). Multiple mechanisms determine the order of APC/C substrate degradation in mitosis. The Journal of cell biology *207*, 23-39.

Mao, H., Hart, S.A., Schink, A., and Pollok, B.A. (2004). Sortase-mediated protein ligation: a new method for protein engineering. Journal of the American Chemical Society *126*, 2670-2671.

Mosadeghi, R., Reichermeier, K.M., Winkler, M., Schreiber, A., Reitsma, J.M., Zhang, Y., Stengel, F., Cao, J., Kim, M., Sweredoski, M.J., *et al.* (2016). Structural and kinetic analysis of the COP9-Signalosome activation and the cullin-RING ubiquitin ligase deneddylation cycle. Elife *5*.

Pettersen, E.F., Goddard, T.D., Huang, C.C., Couch, G.S., Greenblatt, D.M., Meng, E.C., and Ferrin, T.E. (2004). UCSF Chimera--a visualization system for exploratory research and analysis. J Comput Chem *25*, 1605-1612.

Pierce, N.W., Lee, J.E., Liu, X., Sweredoski, M.J., Graham, R.L., Larimore, E.A., Rome, M., Zheng, N., Clurman, B.E., Hess, S., *et al.* (2013). Cand1 promotes assembly of new SCF complexes through dynamic exchange of F box proteins. Cell *153*, 206-215.

Pruneda, J.N., Littlefield, P.J., Soss, S.E., Nordquist, K.A., Chazin, W.J., Brzovic, P.S., and Klevit, R.E. (2012). Structure of an E3:E2 approximately Ub Complex Reveals an Allosteric Mechanism Shared among RING/U-box Ligases. Molecular cell *47*, 933-942.

Qiao, R., Weissmann, F., Yamaguchi, M., Brown, N.G., VanderLinden, R., Imre, R., Jarvis, M.A., Brunner, M.R., Davidson, I.F., Litos, G., et al. (2016). Mechanism of APC/C^{CDC20} activation by mitotic phosphorylation. Proceedings of the National Academy of Sciences of the United States of America 113, E2570-2578.

Reis, A., Levasseur, M., Chang, H.Y., Elliott, D.J., and Jones, K.T. (2006). The CRY box: a second APCcdh1-dependent degron in mammalian cdc20. EMBO reports *7*, 1040-1045.

Scheres, S.H. (2012). RELION: implementation of a Bayesian approach to cryo-EM structure determination. Journal of structural biology *180*, 519-530.

Schrodinger, LLC (2010). The PyMOL Molecular Graphics System, Version 1.3r1.

Scott, D.C., Sviderskiy, V.O., Monda, J.K., Lydeard, J.R., Cho, S.E., Harper, J.W., and Schulman, B.A. (2014). Structure of a RING E3 Trapped in Action Reveals Ligation Mechanism for the Ubiquitin-like Protein NEDD8. Cell *157*, 1671-1684.

Siergiejuk, E., Scott, D.C., Schulman, B.A., Hofmann, K., Kurz, T., and Peter, M. (2009). Cullin neddylation and substrate-adaptors counteract SCF inhibition by the CAND1-like protein Lag2 in Saccharomyces cerevisiae. The EMBO journal *28*, 3845-3856.

Theile, C.S., Witte, M.D., Blom, A.E., Kundrat, L., Ploegh, H.L., and Guimaraes, C.P. (2013). Site-specific N-terminal labeling of proteins using sortase-mediated reactions. Nat Protoc *8*, 1800-1807.

Tian, W., Li, B., Warrington, R., Tomchick, D.R., Yu, H., and Luo, X. (2012). Structural analysis of human Cdc20 supports multisite degron recognition by APC/C. Proceedings of the National Academy of Sciences of the United States of America *109*, 18419-18424.

Wu, S., Zhu, W., Nhan, T., Toth, J.I., Petroski, M.D., and Wolf, D.A. (2013). CAND1 controls in vivo dynamics of the cullin 1-RING ubiquitin ligase repertoire. Nature communications *4*, 1642.

Yamaguchi, M., Yu, S., Qiao, R., Weissmann, F., Miller, D.J., VanderLinden, R., Brown, N.G., Frye, J.J., Peters, J.M., and Schulman, B.A. (2015). Structure of an APC3-APC16 complex: insights into assembly of the anaphase-promoting complex/cyclosome. Journal of molecular biology *427*, 1748-1764.

Yang, M., Li, B., Tomchick, D.R., Machius, M., Rizo, J., Yu, H., and Luo, X. (2007). p31comet blocks Mad2 activation through structural mimicry. Cell *131*, 744-755.

Zemla, A., Thomas, Y., Kedziora, S., Knebel, A., Wood, N.T., Rabut, G., and Kurz, T. (2013). CSN- and CAND1-dependent remodelling of the budding yeast SCF complex. Nature communications *4*, 1641.

Zhang, S., Chang, L., Alfieri, C., Zhang, Z., Yang, J., Maslen, S., Skehel, M., and Barford, D. (2016). Molecular mechanism of APC/C activation by mitotic phosphorylation. Nature *533*, 260-264.

Zheng, J., Yang, X., Harrell, J.M., Ryzhikov, S., Shim, E.H., Lykke-Andersen, K., Wei, N., Sun, H., Kobayashi, R., and Zhang, H. (2002). CAND1 binds to unneddylated CUL1 and regulates the formation of SCF ubiquitin E3 ligase complex. Molecular cell *10*, 1519-1526.